Factors limiting contrail detection in satellite imagery

Oliver G. A. Driver[1], Marc E. J. Stettler[2], and Edward Gryspeerdt[1,3]

[1]Department of Physics, Imperial College London, London, United Kingdom
[2]Department of Civil and Environmental Engineering, Imperial College London, London, United Kingdom
[3]Grantham Institute - Climate Change and the Environment, Imperial College London, London, United Kingdom

Correspondence: Oliver G. A. Driver (o.driver22@imperial.ac.uk)

Abstract. Contrails (~~clouds produced~~ ice clouds, originally line-shaped after initiation by aircraft exhaust) have a significant warming contribution to the overall climate impact of aviation. This makes reducing them a key target for future climate strategies in the sector. Identifying pathways for contrail reduction requires accurate models of contrail formation and lifecycle, which in turn need suitable observations to constrain them. Infrared imagers on geostationary satellites provide widespread ~~,~~ ~~time-resolved observationsof~~ contrail observations, with sufficient time-resolution to observe the evolution of ~~contrail~~ their properties. However, contrails are often narrow and optically thin, which makes them challenging for satellites to identify. Quantifying the impact of contrail properties on observability is essential to determine the extent to which satellite observations can be used to constrain contrail models and to assess the climate impact of aviation.

In this work, contrail observability is tested by applying a simple contrail detection algorithm to synthetic images of linear contrails in an otherwise-clear sky against a homogeneous ocean background. Only (46 ± 2) % of a modelled population of global contrail segments are found to be observable using current 2 km resolution ~~instruments~~satellite-borne imagers, even in this maximally-observable case. ~~A~~ By estimating the radiative forcing of individually-modelled contrails, it is found that a significantly higher portion of contrail forcing is detectable using the same 2 km resolution imager—~~(82 ± 2)~~(72 ± 2) % of instantaneous longwave forcing—because more-easily observable contrails have a larger climate impact. This detection efficiency could be partly improved by using a higher-resolution infrared imager, which would also allow contrails to be detected earlier in their lifecycle. However, even this instrument would still miss the large fraction of contrails that are too optically thin to be detected.

These results support the use of contrail detection and lifetime observations from existing satellite imagers to draw conclusions about the relative radiative importance of different contrails under near-ideal conditions. However, there is a highlighted need to assess the observability of ~~specific contrails depending on the observation requirements of a given~~ contrails where the observation conditions may vary by application. These observability factors are shown to change in response to climate action, demonstrating a need to consider the properties of the observing system when assessing the impacts of proposed mitigation strategies.

1 Introduction

Contrail cirrus is recognised as a significant driver of aviation's climate warming: Lee et al. (2021) suggest it is the cause of more than half the radiative forcing of the sector. Contrail forcing is warming in the longwave (LW), via the cloud greenhouse effect, and cooling in the shortwave (SW), via the cloud albedo effect (Meerkötter et al., 1999). This strong anthropogenic radiative forcing provides impetus for action on contrail mitigation and research.

Early estimates of the radiative forcing due to contrails (e.g. Meerkötter et al., 1999; Meyer et al., 2002) relied on the scaling of radiative transfer simulations to the coverage of linear contrails—measured regionally in satellite observations via either manual identification (Bakan et al., 1994) or by using algorithms for detecting line-shaped ice clouds (Mannstein et al., 1999). The observations use infrared images—particularly split-window brightness temperature images (Lee, 1989)~~which —~~which highlight optically thin ice clouds with small crystals against the surface and background liquid clouds. Both the strong signal and the linearity of the object are used to detect the presence of a line-shaped contrail.

Historically, geostationary satellites did not offer high-enough spatial resolution to detect contrails, as illustrated by the use of imagers on low-Earth orbiting (LEO) satellites for contrail detection (Mannstein et al., 1999; Duda et al., 2013; Vázquez-Navarro et al., 2015). Geostationary observations have the advantage of continuous observation of the same scene with a single instrument, sufficiently time-resolved to observe contrail evolution. Some studies, including Vázquez-Navarro et al. (2015), have identified contrails in LEO satellite imagery before tracking them in geostationary images. Some contrails ~~were only observable~~ detected in LEO imagery were not observable in simultaneous geostationary images, demonstrating an instrument dependence of ~~observablity~~observability. Gierens and Vázquez-Navarro (2018) used statistical approximations to derive that contrails tracked using this technique may be observable for less than half their lifetime, ~~considering~~ due to unobserved parts of the evolution both before and after observation.

Several recent observational studies have demonstrated the ability to detect contrails using modern geostationary satellites (GOES-R series and Himawari 8), including Zhang et al. (2018); Meijer et al. (2022); Ng et al. (2023). ~~This treatment neglects to consider the contrails which remain unobservable by human labellers.~~ These modern satellites have infrared bands used for contrail detection with approximately 2 km resolution at nadir. Initial detection in geostationary images has been found to occur ~~10–30~~ 10–45 minutes after formation ~~(Chevallier et al., 2023; Gryspeerdt et al., 2024)~~(Chevallier et al., 2023; Gryspeerdt et al., 2024; Geraedts et al., 2024), indicating that contrails are unobservable for at least the earlier part of their evolution. Although the contrails are assumed to have small radiative impact during this time, which could be estimated if accurately matched to a generating flight, the delayed onset is an obstacle when attempting to attribute observed contrails to specific aircraft (as was an aim of each of these studies). Each of these studies uses convolutional neural nets to detect the contrails. These rely on datasets of extended line-shaped contrails used as 'training data' to produce an algorithm that is able to detect linear contrails.

~~Kärcher et al. (2009) established that simulated and observed distributions of contrail optical thicknesses differ, and can be reconciled using optical-thickness-dependent detection efficiencies. Previously, studies had focused on relative detection efficiency due to surface inhomigeneities and overdetections due to false positives (Mannstein et al., 1999; Meyer et al., 2002; Minnis et al., 2005; Palikonda et al., 2005; Meyer et al., 2007). The Kärcher et al. (2009) approach goes some way to~~

enabling estimates of contrail coverage which align more closely with model output, albeit with detection efficiency inferred empirically based on the population simulated by the modelEarly studies of linear contrail detection in satellite imagery centre discussions of detection efficiency around the background conditions: surface inhomogeneities driving detection efficiency losses or false-positive overdetections (Mannstein et al., 1999; Meyer et al., 2002; Minnis et al., 2005; Palikonda et al., 2005; Meyer et al., 2007). It is also clear that contrail detectability depends not only on the optical thickness of a contrail, but also the microphysical properties (Yang et al., 2010). Increasingly prevelant Later, Kärcher et al. (2009) established that the properties of the contrail also affect its observability. It was shown that the observed distribution of contrail optical thickness differs from the distribution produced by a model (CCSIM, an analytical model shown to be consistent with large eddy simulations). The observations underestimated the occurrence of optically thin contrails (with optical thickness < 0.2), relative to the model—an empirically-inferred optical-thickness-dependent detection efficiency was able to reconcile model with observation. Although optical thickness ought to be a good predictor of contrail observability, underlying microphysical properties (such as particle size and concentration) will have individual effects on the observability of contrails, depending on the techniques used for their detection (Yang et al., 2010).

The adoption of convolutional neural net algorithms are typically benchmarked against human-identifiable contrails used as training data (Meijer et al., 2022; Ng et al., 2023; Gryspeerdt et al., 2024). If these satellite-observed contrails are to be used to evaluate model simulations on contrails, it is essential that the properties of the observing system are taken into account—a brings with it a new set of limitations to discuss regarding their detection efficiency. These algorithms are typically trained and benchmarked against datasets of contrails identified by humans in satellite imagery, such datasets are also used as 'training data' (Meijer et al., 2022; Ng et al., 2023; Gryspeerdt et al., 2024). Using human-labelled datasets as a benchmark neglects the cases which are unobservable by human labellers (which are likely also unobservable by algorithmic methods), potentially leading to over-estimated detection efficiency.

A concept known as "satellite simulation" (e.g. Bodas-Salcedo et al., 2011) . With can aid in the essential analysis of contrail observability while not depending on the observational limits of a human labeller. These analyses should seek to account for varying instrument propertiesand a , the wide variety of contrail micro micro- and macrophysical properties, and the background conditions; it is not clear that a simple optical depth threshold is suitable for this purpose.

Validation of models, Well-understood observations are required for a large number of reasons, for example, to validate models like CoCiP (the 'Contrail Cirrus Prediction model'; Schumann, 2012)requires well-understood observations. CoCiP produces predictions which generally align with observations , insofar as their properties are resolved (Schumann et al., 2017). CoCiP predictions have been used for predicting contrail formation in order to guide regarding the order of magnitude and principle age-dependencies for micro- and macrophysical properties (Schumann et al., 2017). Planning for in-situ observations (Voigt et al., 2017). CoCiP has been informed by CoCiP applied to forecast data (Voigt et al., 2017). The model has also been used to consider potential consequences of lower non-volatile particulate emissions following climate action, such as due to the adoption of Sustainable Aviation Fuel (SAF) (Teoh et al., 2022b). CoCiP is based on simple, well-understood criteria for formation and persistence, described in Schumann (1996). Most fundamentally, this is driven by Schmidt–Appleman temperature threshold for mixing cloud formationand ice-supersaturation conditions for persistence (with appropriate adaptations,

~~for example, for propulsion efficiency)~~. The properties of the formed contrail are then allowed to evolve, subject to ice water content changes in response to ambient supersaturation, diffusion, and particle number loss processes (Schumann, 2012). Meteorological input limits the predictability of persistent contrail formation, particularly uncertainty in relative humidity values at flight altitudes (Gierens et al., 2020; Agarwal et al., 2022). Model adaptations, such as the correction of ~~relative humidity measurements~~ input relative humidity from meteorology (Teoh et al., 2022a) or alterations to contrail processes like ice crystal formation and loss mechanisms (Schumann et al., 2017) ~~,~~ require well-understood contrail observations for validation.

Beyond model validation, other applications have a varied range of specific observational needs. ~~Climate monitoring and tactical avoidance applications (Geraedts et al., 2023; Chevallier et al., 2023; Sausen et al., 2023)~~ For example, applications include climate monitoring and operational tactical avoidance (action taken in response to current conditions to mitigate the impact of individually-forecast contrails; Chevallier et al., 2023; Sausen et al., 2023; Geraedts et al., 2024). These applications require observation of as high a proportion of strongly forcing contrails as possible (~~and~~ at least at some point in their evolution)~~.~~ ~~The same applications~~ , and often need to match contrails to flights ~~and dynamically avoid contrails~~or take quick action, so observation as quickly after formation as possible is required. ~~Avoidance trials~~ The planning of experimental trials seeking to analyse changes to contrail formation or persistence will benefit from an understanding of the dependence of observability on the properties of contrails and the surrounding conditions, so that they can be confident that unobserved contrails are indeed unformed contrails (Molloy et al., 2022).

This study establishes limits of ~~contrail observability~~ observability for the automated detection of line-shaped contrails as a function of the contrail properties, independently from models. ~~Contrail detection is simulated~~ The detectability of linear contrails is tested in otherwise-clear-sky synthetic ~~radiance fields,~~ satellite images by applying a contrail detection algorithm~~that reflects the contrails visible in context~~. The derived observability threshold will then be compared with ~~a baseline contrail population and its~~ CoCiP-modelled populations of global contrails and their estimated radiative forcing (from Teoh et al., 2024a), and the consequences for a range of applications will be considered. In Section ~~2.1, the simulated contrail images~~ 2, key components of the observability analysis are described, including ~~radiative transfer simulations used to model them . These images are tested using~~ the simulated contrail images and the models used to create them (Section 2.1), the line-filtering ~~detection algorithm described in Section 2.2. A~~ contrail detection algorithm (Section 2.2), and the modelled population of ~~contrails, detailed in Section 2.3, is used to consider the consequences of derived observability thresholds~~global contrails (Section 2.3). Observability assessments are made in Section 3, including varying single parameters (Section 3.1) and ~~derivation of~~ deriving an observability threshold against the key observability-driving properties (Section 3.2)—properties which form a parameter space in which the population of contrails is shown to be well-resolved (Section 3.3). The ~~resulting proportion of contrails and contrail forcing that can be observed are found~~ derived observability threshold is finally applied to the properties of contrails modelled to form in Section 4, resulting in estimates of the observable fraction (Section 4.1), ~~as well as~~ the evolution of this observability with contrail aging (Section 4.2)~~. The validity of radiative importance conclusions made from the observed lifetime is scrutinised in Section 4.3, followed by a consideration of~~ , the lifetime radiative impact of contrails based on their observed lifetime (Section 4.3), and the changing observability as climate action is taken (Section 4.4).

2 Algorithms and data

2.1 Simulated contrail images

The observability of a contrail segment is tested by running a contrail detection algorithm ~~(Section 2.2)~~ over simple simulated radiance fields of synthetic straight-line contrails above a clear-sky ocean scene. The process is outlined in the schematic, Fig. 1~~, and described below~~.

Test contrails are constructed as ~~50~~150 km long cloud segments, with an ice water path (IWP) ~~varied~~ which varies across the contrail in a Gaussian profile. The profile has the form

$$\mathrm{IWP}(s;\, \mathrm{IWP}_0,\, B) = \mathrm{IWP}_0 \sqrt{\frac{4}{\pi}} \exp\left(-\frac{1}{2}\frac{s^2}{B^2/8}\right), \tag{1}$$

describing variations from the ~~contrail IWP~~ charcteristic 'contrail IWP' (IWP_0) across the distance (s) perpendicular to the contrail's length~~(s)~~, given the width of the specific test contrail (B). This is consistent with the optical depth profile used for CoCiP-modelled contrails, described in Schumann (2012). Alongside B and IWP_0, the effective radius (r_{eff}) is another characteristic contrail property (describing the size of constituent ice crystals). Each synthetic contrail is assumed to have constant r_{eff}. In reality, contrails are not straight lines, and their properties and evolution may vary along their length. The consequence of such variations is considered in this work by using the detectability of these test contrails to inform the observability of modelled contrail 'segments', the overall contrail's properties may vary from segment-to-segment.

A 1-D radiative transfer simulation using the US standard atmosphere is run at each point in the test contrail, on a 0.25 km grid, to produce a radiance field (at 'high-resolution' relative to satellite imager output), from which brightness temperatures are calculated. The DISORT algorithm (Buras et al., 2011) was used for radiative transfer calculations, as implemented in the libRadtran library (Emde et al., 2016), with the pyLRT python wrapper (Gryspeerdt and Driver, 2024) used to perform the simulations. The ice water content and ~~droplet~~ size distribution are assumed uniform across the contrail depth. When $r_{\mathrm{eff}} > 5$ µm, the contrails are parameterised using the Yang et al. (2013) parameterisation as distributed with libRadtran, using smooth droxtal (faceted spheroid) habits. The lower-limit on r_{eff} is a limit of this parameterisation. To simulate contrails with smaller ice crystals, absorption coefficients were calculated using the 'mie' package (also distributed with libRadtran) for spherical ice crystals with a Gamma distribution of particle radii consistent with the libRadtran microphysics implementation. The viewing zenith angle has been taken to be zero, introducing an assumption that observation occurs near the satellite's nadir. The surface is assumed to have unit thermal emissivity (similar conditions to the ocean), and the surface temperature is treated as 15 °C (a property of the temperature profile). GOES-ABI imager bands are simulated using the REPTRAN representative wavelength parameterisation (Gasteiger et al., 2014). ~~Additional radiative transfer simulations are made of contrails against a layer of cirrus background, as well as the baseline sythetic observations which are made in otherwise-clear sky. The background cirrus layer is 500 m deep, at 8 km altitude, with an effective radius of 5 µm (chosen as the intersection of the two ice cloud parameterisations due technical limitations) and IWP of 25 gm^{-2}. The layer has an optical thickness of approximately 3.~~

For computational efficiency, a lookup table of brightness temperature values for a comprehensive range of contrail physical properties was used to produce the simulated brightness temperature fields. The radiative transfer lookup table is based ~~in~~ on a

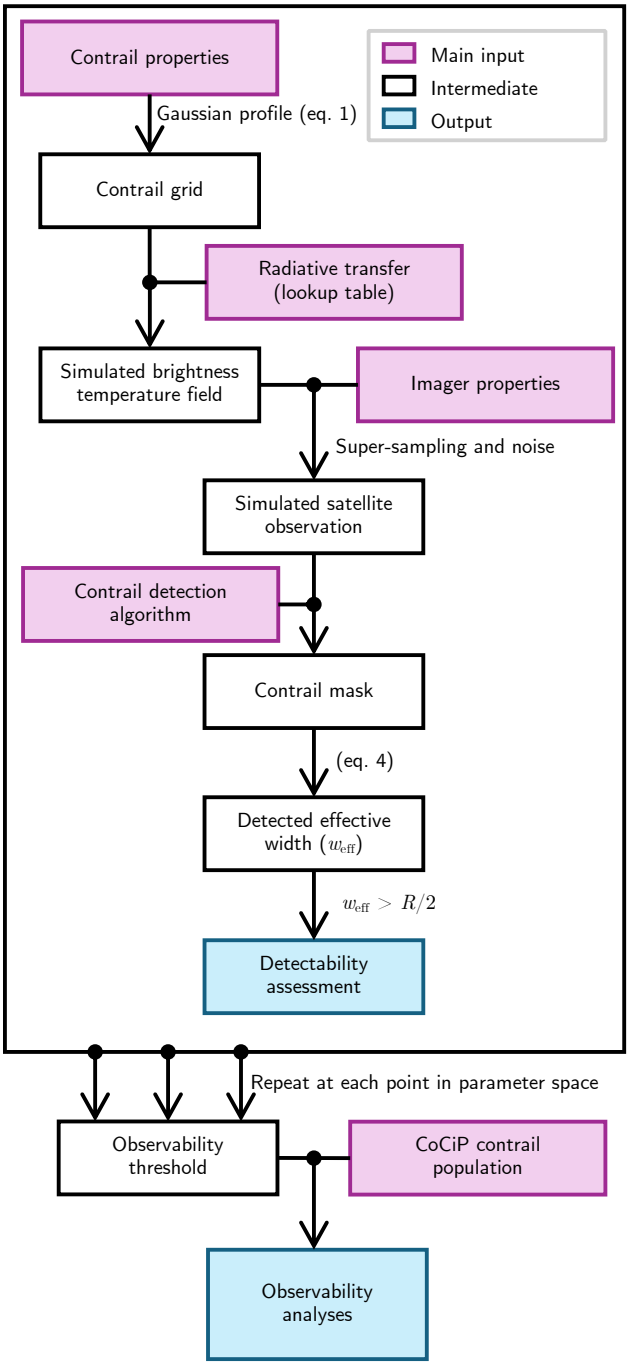

Figure 1. ~~The~~ Schematic of the process for deriving ~~the probability of observation detected~~ contrail detection efficiency by ~~repeated~~ application of a contrail detection algorithm to synthetic observations of a single contrail, using a ~~specified~~ specific imager ~~,~~ and contrail detection algorithm, and ~~calculated~~ a pre-calculated radiative transfer lookup table.

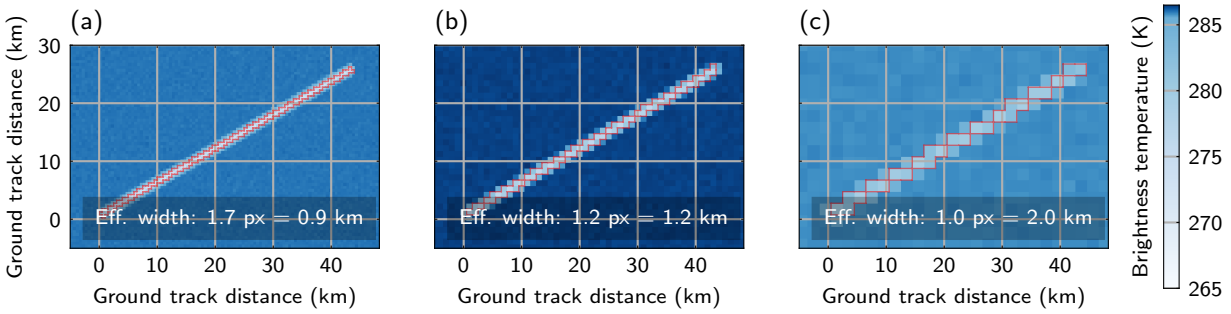

Figure 2. Example simulated observations of 50 km long contrails~~used for theoretical observability testing~~, imitating imagers with (a) 0.5 km, (b) 1 km, and (c) 2 km surface spatial resolution. Values are brightness temperatures as observed using the profile of the GOES-ABI band 14 (centred on 11.2 µm). Red line denotes the contrail mask detected. Note the skewed colour scheme intended to simultaneously highlight imager noise and decreased peak brightness temperature with the coarsening resolution. Image-to-image variability is given by a simulated calibration error (sampled for each realisation from a Gaussian with standard deviation 0.2 K), and pixel-to-pixel by the NEdT (sampled for each pixel from a Gaussian with standard deviation 0.03 K).

parameter space grid, linearly-spaced in IWP (between 0 and 100 g m^{-2}), r_{eff} (between 0.1 and 80 µm), contrail depth (between 50 and 1500 m), and altitude (between 6 and 13 km). Linear spacing of the lookup table includes more gradual variations in simulated radiances than a lograrithmically spaced parameter grid, so is better suited for interpolation where required.

The high-resolution simulated brightness temperature field is then processed to simulate the properties of a given imager, coarsening the resolution and applying measurement noise. The brightness temperature grid is coarsened to a grid given by the imager's resolution, using a conservative local-mean downgridding technique (to integer multiples of the high resolution grid). A Gaussian noise with standard deviation equal to a noise-equivalent temperature deviation (NEdT) of 0.03 K is applied to simulate the pixel-to-pixel uncertainty—approximately equivalent to the GOES-ABI NEdT based on on-orbit tests of GOES-16 (NOAA, 2019; Wu and Schmidt, 2019). Multiple realisations of the brightness temperature field are produced, each offset with a single calibration error sampled ~~for~~ from a 0.2 ~~K—representative~~ K wide Gaussian—representative of the image-to-image uncertainty of the GOES-ABI imager (NOAA, 2019). ~~Fig. 2 shows simulated~~ Examples of such synthetic brightness temperature fields ~~for the GOES-ABI band 14 (centred on 11.2 µm) for~~ are shown in Fig. 2.

Radiative transfer modelling of contrails has been previously performed by Schumann et al. (2012); Wolf et al. (2023). Both these previous works similarly use libRadtran (Emde et al., 2016) to perform calculations. Each use similar ice cloud parameterisation settings to this work, with Schumann et al. (2012) using an earlier set of scattering properties. The previous works similarly suffer from a lack of scattering properties for small crystals, and the Schumann et al. (2012) work turns to Mie calculations for this purpose, as is done in this work. For larger crystals, each of the two previous works choose to use a range of ~~resolutions.~~ different habits which may be found in contrails—this was omitted here with the aim of choosing a habit that was consistent with the Mie calculations. Similarly, the other works use a range of atmospheric profiles. The approach taken here is aligned with the aim of considering an idealised case to provide an upper limit of the detectability; variation in

habit mixtures and atmospheric profiles will add further variability to the detection efficiency achievable in practice. The other works have additional considerations for solar radiation, including solar zenith angle variations—neglected in this work due to the focus on thermal radiation for the detection algorithm used.

2.2 Contrail detection algorithm and observability criteria

A simple convolutional filtering contrail detection algorithm is applied to the images. The detection algorithm used is based on the implementation of the Mannstein et al. (1999) algorithm~~distributed with~~ , as implemented by McCloskey et al. (2021). This is a line-filtering algorithm, applied on infrared brightness temperature fields. Brightness temperature (using the 11.2 µm band of the GOES ABI instrument) and brightness temperature difference (between the 10.3 and 12.3 µm bands of the same instrument) fields are used for contrail detection. The fields are lowpass-filtered, differenced from a smoothed version to extract the signal, normalised, and clipped of extreme values. A threshold is applied to each of the two fields, as well as a combined field convolved with line filters in a range of different directions. For the McCloskey et al. (2021) implementation, the thresholds have been tuned on a human-labelled dataset, establishing the contrails detected using this algorithm as representative of those observable by human labellers. ~~The change resulting from altering these thresholds to detect contrails producing a minimally-detectable signal against imager noise are briefly considered in Section 4.1, although this would require controls to mitigate the risk of false positive detections in real observations (e.g. targeted observation of a specific contrail)~~The detection algorithm produces a binary mask of pixels detected as being 'contrail'.

The algorithm has been minimally adapted in this work to relieve some emergent issues. The algorithm was found to selectively omit contrails aligned with the dimensions of the simulated imager grid, a result of using the r-squared statistic as a test for linearity. A linearity score was devised to replace the r-squared statistic,

$$\epsilon^2 = 1 - \frac{\sum d_\perp^2}{\sum d_\parallel^2}, \tag{2}$$

where $d_\perp$ is the perpendicular distance to a pixel from a linear fit to the masked points, and $d_\parallel$ the distance between a masked pixel and the midpoint of the line, and sums act over each of the pixels in the detected area. ϵ is the eccentricity of an ellipse whose semi-major and semi-minor axes are the mean $d_\parallel$ and $d_\perp$ respectively. This relieves the dependence on axes arbitrarily chosen relative to the contrail.

Detected contrails were also checked for their alignment with the simulated contrail. Regions whose orientation differed from the simulated contrail by $\pm$ 30° are neglected. This removes artefacts where the 'end' of the contrail has been detected, but not the main body of the contrail. This is a result of the contrail profiles terminating suddenly, producing a regional gradient in brightness temperature fields, ~~highlighted by the Mannstein et al. (1999) style detector~~which is picked out by the detection algorithms used in this work. This only arises for very wide, optically thick simulated contrails, ~~it is not a measure that would ever be required for operational contrail detection of physically realistic contrails~~due to their physically unrealistic profiles; such a condition would never be needed in operations on real observations.

The algorithm produces a mask of contrail pixels from an image, of area

$$A_{\text{mask}} = N_{\text{px}} R^2, \tag{3}$$

where N_{px} is the number of masked pixels and R the imager resolution. The presence of a contrail has been accurately detected if the mask is made up of at least one pixel along the length of the contrail. It is useful to consider the width of the area detected as a contrail, because an imager is only able to detect an area in units of pixels. We define the 'effective width' as

$$w_{\text{eff}} = \frac{A_{\text{mask}}}{l} \Rightarrow \frac{w_{\text{eff}}}{R} = \frac{N_{\text{px}}}{l/R}. \tag{4}$$

A one-pixel effective width ($w_{\text{eff}} = R$) corresponds to a minimally detected contrail along the whole length (l) of the contrail. For each simulated contrail detection attempt, a threshold $w_{\text{eff}} > R/2$ is applied, such that a detection along most of the length, but not neccessarily all, is accepted. This minimally-restrictive condition ensures that very narrow contrails whose ends are omitted from the mask are not penalised as failed detections. ~~Observability is tested against this condition using four different realisations of the instrument noise, before aggregating the probability of detection (P_{obs}) for a particular set of cloud properties. An 'observability threshold' is then determined in the parameter space, for contrails with $P_{\text{obs}} > 0.5$. P_{obs} thresholds of 0.25 (detected in one realisation) and 0.75 (detected in all but one realisation) are used to indicate the uncertainty in the observability threshold. This is only a small contribution to the uncertainty in later-derived fractions of observable contrails compared to seasonal and diurnal variability in the properties of the contrails in the population and their estimated radiative forcing.~~

2.3 The distribution of "real" contrail properties

A ~~baseline~~ reference population of contrails and their properties is needed to analyse whether the most climatically relevant contrails are observable: those which form and persist, and those which cause the most radiative forcing. To avoid the observational biases in the population of contrails, a modelled inventory of contrails is used.

The CoCiP-derived contrail dataset of Teoh et al. (2024a) provides a global inventory of contrail segments globally at 5 minute intervals, derived from air traffic data. These segments are the result of the application of CoCiP for flights in 2019–2021, produced using the pycontrails implementation of the model in Python (Shapiro et al., 2023), including radiative forcing estimates based on the parameterisation of Schumann et al. (2012). Air traffic is based on the GAIA emissions inventory (Teoh et al., 2024b), which showed good agreement with other flight inventories, and showed only a small deficit compared to major airport statistics. This population of contrails should not be expected to match observations on a flight-by-flight basis. It is produced using the ERA5 meteorological ~~reananlysis~~reanalysis, which has difficulty producing accurate ice-supersaturation fields at flight altitudes (Gierens et al., 2020). However, it is ~~expected~~ assumed that the statistics of this population are aligned with the population of actual contrails. ~~This database is suitable for this study because contrail observability is to be tested independently of the specific meteorological context. The following analysis is based only on the distribution of contrail properties which drive observability to first-order.~~

Two populations are used for different parts of this work:

1. The '~~instantanous~~instantaneous' sample, constructed from global contrail datasets at 114 timesteps randomly-sampled through 2019, with minimum separations of 24 h. This is approximately 14 million contrail ~~waypoints~~ segments in total. The timestamps are well-distributed seasonally and throughout the day, so are representative of seasonality and the diurnal cycles of ~~warming~~ meteorology, forcing, and air traffic.

2. The time-resolved dataset, wherein the properties of all contrail segments that formed in a 24 h period between 1200 UTC on ~~2024-01-06 and 2024-01-07~~ 2019-01-06 and 2019-01-07 were tracked for their whole lifetime, up to 12 h after their formation (at which time they would be removed by CoCiP). Around 1 million contrail segments are formed in the 24 h window, forming a dataset of 34 million segments as they evolve.

The contrail data is analysed as a set of contrail segments—partial lengths of contrail which form over 5 min intervals. This supports the analysis of geometrically extended contrails with varying meteorological conditions and properties along their length. Each contrail segment persists in the CoCiP model until one of a range of end-of-life conditions is met, including optical depth, ice crystal number concentration, and altitude thresholds, or if their age exceeds 12 h, detailed in Teoh et al. (2024a). The length of time for which a contrail segment remains in the model is termed the 'persistence lifetime' for this work.

~~Some variability in the properties of the contrail population is caused by seasonal and diurnal variations in both meteorology and air traffic. The extent that this variability leads to changing contrail observability is tested by subsetting the instantaneous sample (population 1) by month and 'daytime' contrails (0600–1800 local solar time) and 'nighttime' contrails (1800–0600 local solar time). Using globally-consistent thresholds, rather than local solar time, highlights variability in the instantaneous contrail population globally rather than the local conditions. The standard deviation in observability fractions derived on each of these subsets is used as an uncertainty caused by seasonal and dirunal variability.~~

CoCiP is not a perfect model, and some flaws in the distribution of contrails are ~~clear~~ apparent in the red histograms of properties from the CoCiP population shown in Fig. 3. These include a high frequency of contrails at the maximum depth in Fig. 3(e) (1.5 km) and the occasional occurrence of very wide contrails in Fig. 3(c) for which assumptions of linearity and homogeneity across the width are likely to break down. Nonetheless, the model has found broad-based application (Jeßberger et al., 2013; Schumann et al., 2015; Voigt et al., 2017; Teoh et al., 2020, 2024a), and the population of contrails produced has been shown to align with in-situ and satellite observations (Schumann et al., 2017; Voigt et al., 2017).

3 Contrail parameter observability tests

3.1 Single parameter sensitivity tests

~~Contrail IWP~~IWP_0, r_{eff}, width, altitude and ~~width~~ depth were each varied while holding other properties constant. The impact on the detected w_{eff} (~~equation~~ eq. 4) of these parameters is shown in Fig. 3~~, with the mean effective width across four realisations, $\overline{w_{\mathrm{eff}}}$, shown with the solid line, and individual w_{eff} measurements shown as scatter points. $w_{\mathrm{eff}} = R_f/2$ thresholds for detection are shown as dashed lines.~~.

In each observability test, properties are varied with respect to a baseline contrail, which is 2 km wide, 0.5 km deep, has a base altitude at 11 km, r_{eff} of 10 µm, and ~~IWP~~ IWP_0 of 2 g m^{-2}. The baseline properties are chosen as representative of ~~the instantaneous contrail sample of Section 2.3 (~~global contrail properties (based on CoCiP population 1)~~, histograms of which are shown alongside the observability response. The r_{eff}, IWP and width of this baseline contrail are marked with a blue cross~~

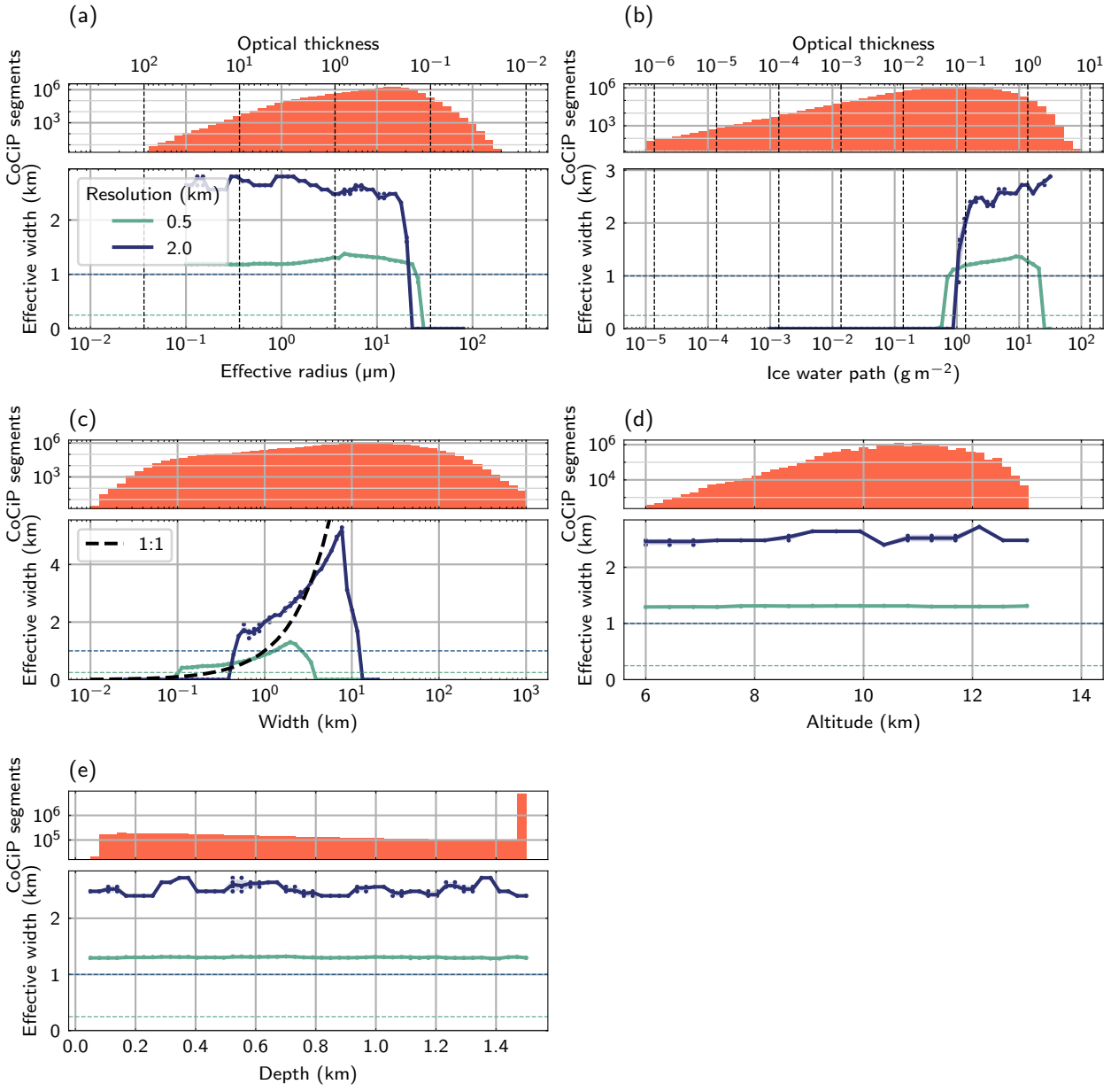

Figure 3. Tests for changes in contrail observability (i.e. observed effective width) when varying r_{eff} (a), ~~IWP~~ IWP$_0$ (b), width (c), altitude (d) and depth (e) of contrails. Blue-green solid lines are the average w_{eff} detected ~~w_{eff} averaged~~ over 4 noise realisations for two different imager resolutions, with scatter points the individual measurements. The corresponding dashed lines are the $w_{\text{eff}} \geq R/2$ condition for detection. The response is plotted alongside histograms of ~~the~~ global contrail properties (from CoCiP ~~model~~ population ~~'s properties~~ 1). ~~Based on the instantaneous contrail sample.~~ A black dashed line in panel (c) indicates equal w_{eff} and prescribed contrail width.

~~in histograms of this population Fig. 5(b, c).~~ . This analysis is intended to abstract the observability consequence of the each individual contrail property from the consequence of the others, so no attempt is made to ensure that contrails simulated in the course of these observability tests are realistic, including no accounting for properties which are likely to covary (such as width and depth).

There is a low-optical-depth observability limit seen in the high-r_{eff} and ~~low-IWC~~ low-IWP$_0$ regimes of Fig. 3(a,b)—as expected, contrails which are too optically thin are unobservable. Very optically thick contrails also appear undetectable, creating a ~~high-IWP~~ high-IWP$_0$ limit of observability seen for the 0.5 km resolution imager in Fig. 3(b). This ~~high-IWP~~ high-IWP$_0$ limit occurs when the centre of a contrail becomes so optically thick as to appear opaque to the upwelling thermal radiation in both imager channels which are differenced for the brightness temperature difference signal (used for contrail detection, Section 2.2). The analogous limit for the coarser-resolution imager is not seen, despite the expectation that the opacity as a function of IWP is resolution-independent. The limit occurs at higher IWP$_0$ for the coarser-resolution imager because the effect of the peak IWP at the centre of the profile is 'averaged' over the pixel, which would include some lower-IWP of the profile (eq. 1) further from the centre. For this contrail, with this particular width, the signals in the synthetic image are simply not strong enough to cause a detection.

A significant observability response occurs as contrail width is increased, shown in Fig. 3(c). The narrowest contrails are not detected, with an observability onset occuring as contrail width increases to (slightly below) the imager resolution. ~~$\overline{w_{\text{eff}}}$~~ The w_{eff} detected then increases from an initial approximately one-pixel effective width, detecting the broadening contrail. Note that ~~a directly comparable contrail width is not straightforwardly produced~~ the measured contrail widths differ when the same contrail is imaged using imagers with different spatial resolutions. The same underlying contrail produces contrails of different pixel mask areas, so ~~different $\overline{w_{\text{eff}}}$ and inferredwidth~~a different w_{eff} is inferred. This is ~~analagous~~ analogous to the dependence of cloud fraction on the resolution of a binary cloud mask, found by Shenk and Salomonson (1972).

Wide contrails are also not detected. This is a limitation of the detection algorithm used—which uses line kernels that highlight linearly-extended regional gradients 1–4 pixels wide. The CoCiP population has a significant spread in width, including contrails with widths of up to several hundred kilometres, so this algorithm limitation would have a significant effect if untreated. ~~These wide unobservable contrails are~~ Detection occurs within different upper- and lower-limits of width for each of the imagers tested. The high-width limit is likely to be ~~detectable~~ overcome if a different approach is used, given that narrower contrails with similar microphysics ~~have been identified~~ are detectable using this algorithm. ~~To assess the impact of a less conservative contrail detection algorithm, detectability thresholds are adjusted to only include low-width unobservability behaviour, detailed in Section 3.2 (the adjusted threshold in Fig. 5).~~ For example, the observation could be downsampled onto a coarser grid before applying the detection algorithm. As a result, it is reasonable to consider all contrails wider than the narrowest-detectable contrail with a given set of microphysical properties to be detectable.

~~The contrail~~A contrail's altitude is expected to limit the brightness temperature contrast between the contrail and clear-sky regions of an image, limiting observability. However, contrail altitude is not found to have a significant effect on the observability of this particular baseline contrail (Fig. 3(d)). ~~This~~ In fact, the altitude effect only becomes important when contrail width is less than the imager resolution, as shown in Fig. 4, where detectability has been tested at a range of altitudes

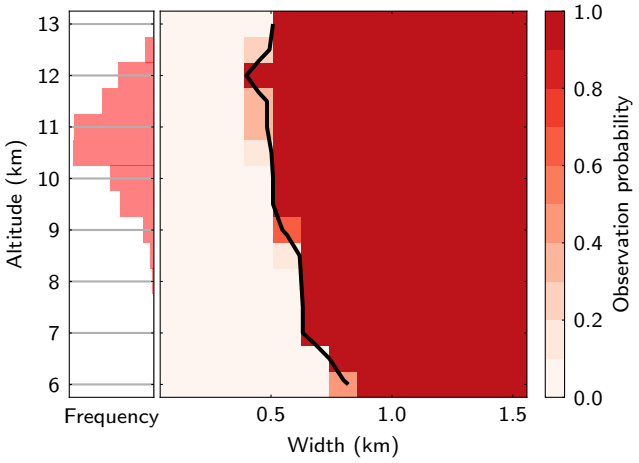

Figure 4. The observability of contrails at different altitude as width ~~with respect to the baseline contrail~~is varied. Tested for a simulated 2 km resolution imager for ten realisations of a synthetic noise field. The black contour shows the resulting observability threshold.

for contrails with sub-grid widths~~over ten noise realisations~~. The detection probability is shown to co-vary with altitude and width, for contrails with width significantly below the imager's resolution (of 2 km). Higher contrails have greater brightness temperature contrast with the background than lower contrails, so become observable at narrower widths ~~(as discussed in Section 2.1 and Mannstein et al., 1999)~~(discussed in Mannstein et al., 1999), however this effect is small for the altitudes at which contrails form.

The vertical depth over which the contrail's IWP is spread also does not drive a strong observability response (Fig. 3(e)). This relaxes any observability bias that may emerge from the unrealistic distribution of contrail depths in the CoCiP histogram of Fig 3(e).

3.2 Contrail observability threshold

~~IWP, r_{eff}, and contrail width~~ The analysis of Section 3.1 leads to the identification of a parameter space consisting of those properties which have a strong control on contrail observability~~(Fig. 3). This aligns with expectations: contrail observability ought to depend on the contrail optical thickness (to first order, a combination of r_{eff} and IWP), and the interaction of the contrail's geometry with the imager's pixel resolution. A sensitivity to altitude was also observed for narrow contrails~~: IWP_0, r_{eff}, and contrail width. The observability of a contrail is tested in this parameter space by covarying these three parameters. The population has been split into logarithmically-spaced bins in each dimension—including contrail width bins between 0.025 and 25 km wide, r_{eff} bins between 0.1 and 50 µm, and IWP_0 between 10^{-3} and $10^{3/2}\ \text{g m}^{-2}$. We neglect altitude variations, because it only had a weak observability effect (Fig. 4), ~~although dependence on altitude is weak at the higher altitudes where most contrails exist. An altitude~~ so an altitude of 11 km ~~has been~~ is assumed for all ~~contrails—this~~ contrails. This altitude is approximately consistent with the modal altitude (Fig. 3(d)), and aligns with the aim of a maximally-observable case (Fig. 4). ~~The observability of a contrail was tested in the identified parameter space: covarying IWP, r_{eff}, and width. Histograms in~~

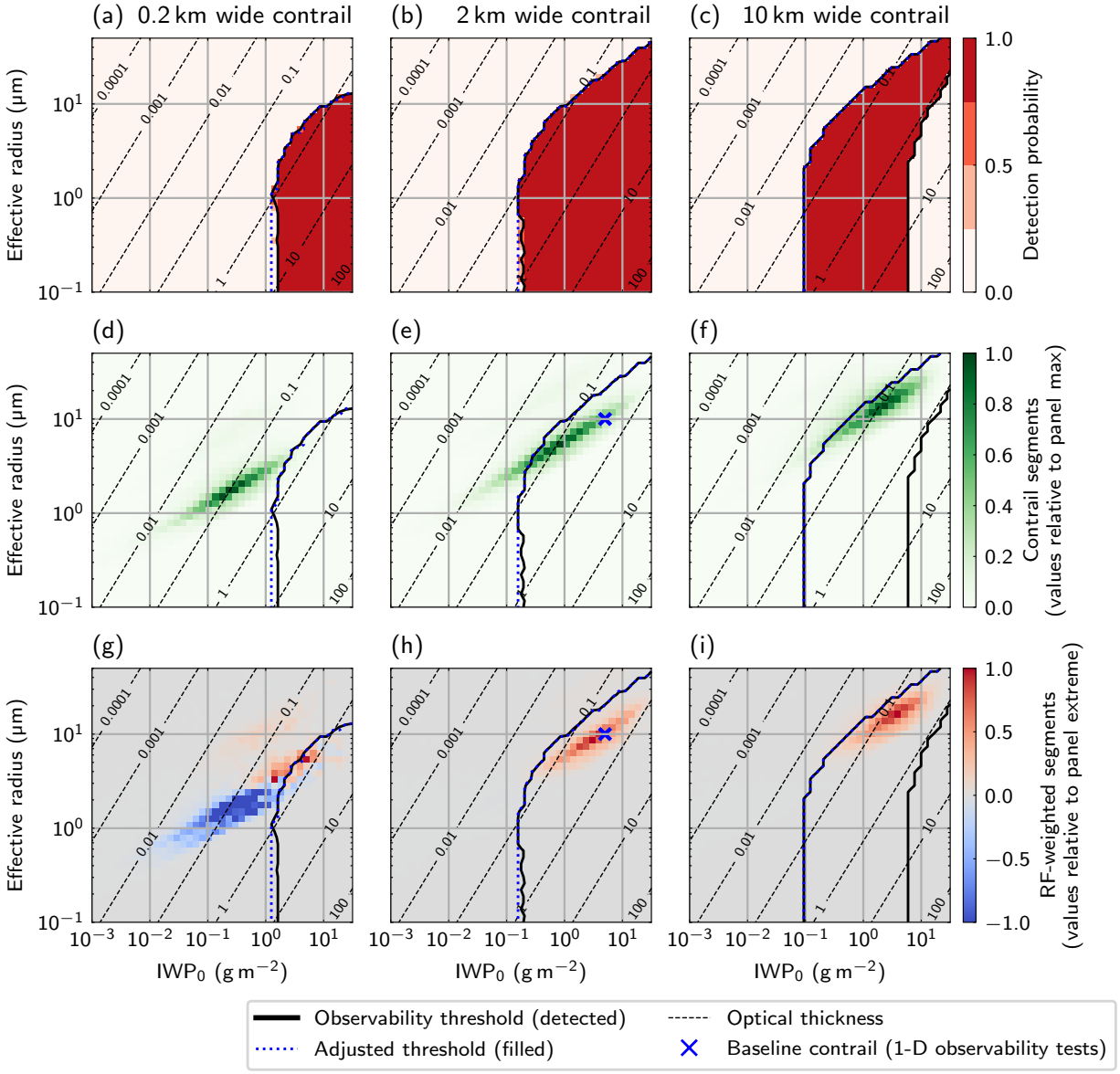

Figure 5. Illustrative slices from a ~~3-D~~ contrail observability test ~~, including~~for three contrail-width bins (chosen from 30 total bins): ~~observability quantified using effective width~~ 0.2 km- (a, d, g), ~~and histograms of CoCiP populations weighted by occurrence~~ 2 km- (b~~)~~, e, h) and ~~net radiative forcing~~ 10 km-wide (c~~)~~, ~~for 2 km wide contrail segments~~f, i) contrails. ~~Similar~~ The observability threshold is plotted over the derived detection probability (a–c), and histograms ~~are shown for 0.2 km wide contrails~~ of CoCiP population 1 (~~d~~d–f) and ~~15 km wide~~ of the same population weighted by the mean net RF of the contrails in each bin (~~e~~g–i). The histogram values (d–i) are relative to the magnitude of the extreme value in each plot. The 'adjusted threshold' represents the observability threshold adapted to include all theoretically observable contrails, without the high-width algorithm deficiency. Contours of the contrail optical thickness (estimated based on IWP$_0$ and r_{eff}) are also shown.

this space at constant width are shown in Fig. 5, alongside a derived observability threshold. The population has been split into logarithmically-spaced bins in each dimension—including contrail width bins between 0.025 and 25 km wide. Slices of these histograms at contrail widths narrower than, comparable to, and wider than imager resolution have been shown—illustrative of different observability behaviours. The logarithmic scale is most appropriate for resolving the width distribution and observability threshold (as in Fig. 3(c)

Detection was performed on four realisations of the synthetic radiance field for each set of contrail properties, testing the measured w_{eff} (eq. 4) against the condition for detectability ($w_{\text{eff}} > R/2$). A 'probability of observation' p_{obs} is then derived (the proportion of noise realisations with a 'detectable' outcome). The detectability threshold is then the surface bounding the region in the parameter space where $p_{\text{obs}} > 0.5$.

Fig. 5(a, b, and c) are observability test results for contrails approximately)–(c) shows the observability threshold derived for a GOES-ABI-like 2 km wide, in images using a simulated 2 km resolution imager . In for three different width bins in this parameter space. The chosen widths illustrate the different observability behaviour of contrails narrower-than, comparable-to, and wider-than the imager resolution. Histograms showing the distribution of CoCiP population 1 contrail r_{eff} and IWP_0 are shown in Fig. 5(a), the detection probability is shown as a function of the parameter space . d)–(i), alongside the derived threshold. The choice of parameter space and logarithmically-spaced bins enables both these distributions and the threshold to be clearly resolved.

Contrails with a larger optical thickness tend to be more observable than those with a lower optical thickness. The observability threshold, $P_{\text{obs}} > 0.5$, is shown as a black contour. Fig. 5(b) shows the observablity threshold with the distribution of contrail segments with approximately this width, taken from the instantaneous contrail sample. Fig. 5(c) is as Fig. 5(b), with the population weighted by the net radiative forcing. For these 2 km contrails, the observability threshold splits the population (Fig. 5(b)), but the segments generating strong radiative forcings are generally observable (, aligning well with expectations. Regardless of contrail width, contrails with optical thickness below approximately 0.05 were found to be undetectable, consistent with past work (e.g. Kärcher et al., 2009). Additionally, the detectability of more optically thick contrails is seen to depend on the specific properties—particularly the contrail width, as well as r_{eff} and IWP_0. An apparent exception to the high optical thickness observability emerges at high width, where the most optically thick contrails appear undetectable. This is an artefact of the same high-width limit of detection discussed in Section 3.1. We adjust the threshold to make the subsequent analysis applicable to detection algorithms without this deficiency. This is achieved by treating the threshold as defining a 'minimum width' given by the narrowest contrail with each r_{eff} and IWP_0 that is detectable. This adjusted threshold is shown using the dotted blue contour in Fig. 5(c)).

For contrails significantly narrower than the imager's resolution, a higher contrail optical thickness is required to detect the contrail (Fig. 5(da), compared to (a, eb, c)). CoCiP population 1 contrails in the 0.2 km width bin (Fig. 5(d)) are mostly 'too narrow' to be detected, as is much of their forcing (Fig. 5(g)) A wider contrail with the same properties would be detectable. It is notable that sub-pixel-width contrailsthese contrails, which are less than one pixel wide, can still be observable, but that any single no width-independent 'optical thickness threshold' is insufficient for characterising contrail observability. Observability

~~also depends on both the contrail microphysical and geometrical properties, especially the contrail width relative to the imager resolution.~~ can be used to define observability.

~~When tested against contrails wider than the imager's resolution (shown for~~ The CoCiP population 1 contrails and net contrail forcing in the 10 km ~~wide contrails in Figure 5(e)), contrails are markedly less detectable, corresponding to the high width unobservability observed in Section 3.1~~ bin are mostly observable (Fig. ~~3(e~~5(f, i)). ~~Optically thick wide contrails are preferentially undetected compared to more optically thin ones at the same width—this is because the more optically thin contrails can be detected as a narrower contrail by detection of only the central part where the IWP peaks. As discussed in Section 3.1, this high-width undetectability is a property of the detection algorithm used. The observability threshold is adjusted to treat all contrails wider than the narrowest detected contrail with the same IWP and r_{eff} as detectable. This adjustment is shown using the dotted blue contour in Fig. 5.~~

~~The 'cause of unobservability' for an unobservable contrail with a given set of properties is also defined in terms of the adjusted 'theoretically observable' (blue dotted) threshold derived here. Any contrails for which there exists a wider, theoretically observable contrail with the same IWP and r_{eff} (therefore, the same peak optical thickness) are deemed 'too narrow', other unobservable contrails are 'too~~ However, there is a significant proportion of contrails and their forcing which does remain outside the adjusted threshold at these high widths. Such contrails (where there is no width in the parameter space that would make a contrail with that r_{eff} and IWP_0 detectable) are 'too optically thin' to be detected.

3.3 Principal components of variability in the parameter space

Through the 1-D analyses of Fig. 3, it is clear that the observability is a strong function of the three parameters used for the observability space (~~IWP~~IWP_0, r_{eff}, and width). The histograms of Fig. 5(~~b, c, d, and e~~d–i) suggest that the CoCiP population approximates a plane in this space (on logarithmic axes). This behaviour is important to ~~enable robust application of~~ make sure the derived observability threshold is robust to any variability in the contrail properties.

Principal component (PC) analysis (Lever et al., 2017) can indicate the key directions of variability, and the amount of population variability which exists in these emergent directions. Examining the PCs and their associated proportion of variance enables us to establish to what extent the population lies on ~~on~~ a plane in this space, and the principal components offer some physical insight. Values of ~~log(IWP)~~$\log(\text{IWP}_0)$, $\log(r_{\text{eff}})$, and $\log(\text{width})$ are standardised to have unit variance before analysing because of their different scales.

Fig. 6(a) shows the principal components within this parameter space, and Fig. 6(b) shows the associated proportion of the variance. Together, PC0 and PC1 describe 96 % of the variance of the population. PC0 is a component describing ~~IWP~~IWP_0, r_{eff} and width covarying—i.e. bigger contrails tend to be more optically thick, presumed to be related to the temporal growth of the contrail. PC1 comprises anti-correlated ~~IWP~~ IWP_0 and width, at approximately constant effective radius—this can be interpreted as contrail segments at a different point in their evolution, with the fixed population of ice crystals being spread over a growing width as a segment ages. ~~The correspondence of these principal components to the time-evolving properties of the model population are illustrated in the below analysis of population 2 (Fig. 8).~~

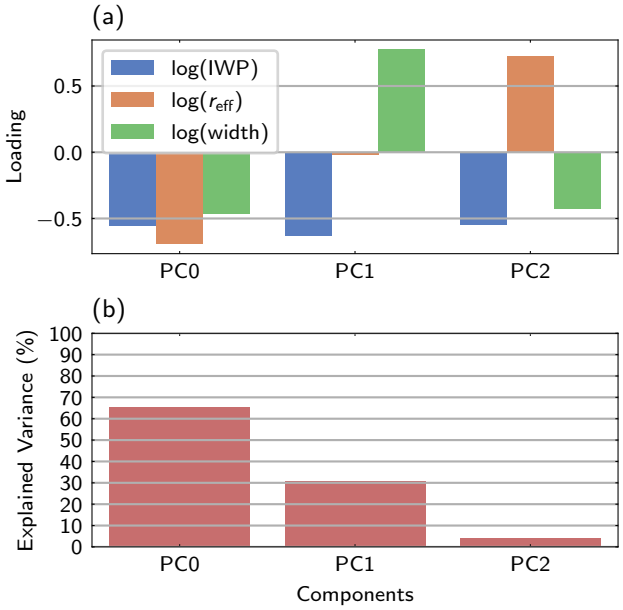

Figure 6. The principal components (PCs) of the CoCiP population in an ~~IWP~~–IWP_0–r_{eff}–width parameter space. (a) shows the PC loadings with each variable, and (b) shows the percentage of variance explained by variability in the direction of this PC.

4 Population observability consequences

4.1 Contrail segment observability

4.1.1 Idealised detection efficiency estimates and uncertainty

Fig. 7 shows the percentage of contrail segments which are observable using simulated 0.5 km~~and~~ , 2 km, and 7 km resolution imagers. The observable fractions are based on the combination of ~~the instantaneous contrail sample described in Section 2.3 (~~CoCiP population 1 ~~)~~ and the observability threshold found in Section 3.2, including the ~~wide-contrail correction. (46 ± 2) % of contrail segments are observable in~~ adjustment for wide contrails. The thresholds are shown in Fig. 8(a–c), as the minimum width required for detection of a contrail as a function of r_{eff} and IWP_0. The 2 km resolution ~~satellite images~~is most representative of the current generation of geostationary imagers (like GOES-ABI), so is the focus of this discussion. The coarser resolution is chosen as a point of comparison, this resolution is achieved by previous-generation geostationary imagers at mid-latitudes (e.g. MSG-SEVIRI).

In 2 km resolution satellite images (46 ± 2) % of contrail segments are found to be observable, this increases only 7 percentage-points when a 0.5 km imager is used. ~~Examining the causes of unobservability, the observability gain~~ The observability gain from the higher resolution is minimal because the significant majority of unobservable contrails are too optically thin to be observed, rather than too narrow. Optically thin contrails are not as accessible via imager resolution enhancements—observations

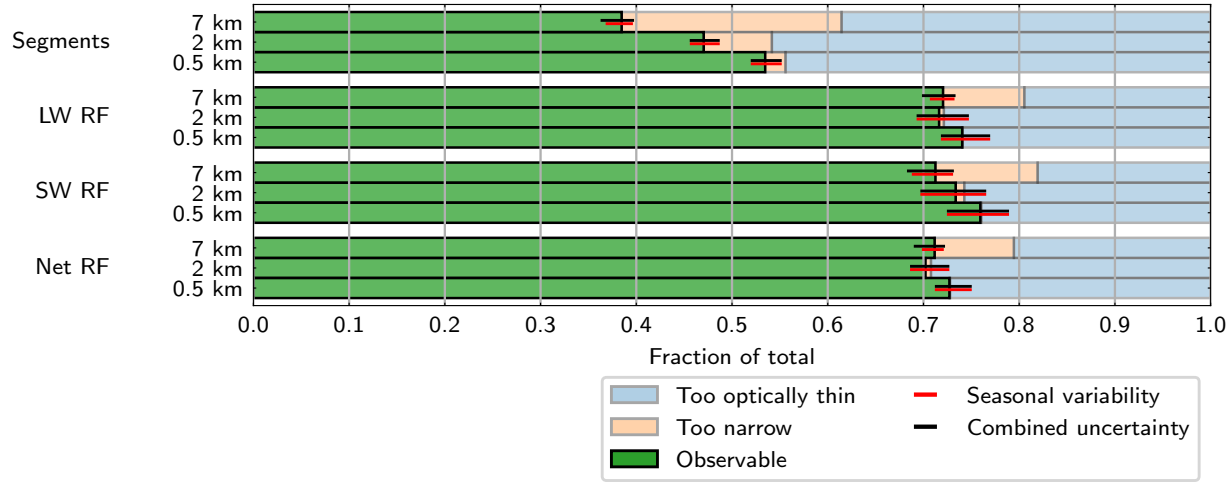

Figure 7. The fraction of contrail segments that are theoretically observable ~~fraction~~ using imagers with 7, 2, and 0.5 km spatial resolution. Shown as a proportion of contrail segments, and weighted by their instantaneous ~~SW,~~ LW, SW, and absolute net ~~radiative forcing, based~~ RF (per unit length). Based on the distribution of properties modelled in CoCiP ~~populations~~ population 1 using Jet-A1 fuel. Unobservable contrails are categorised as either too narrow or too optically thin to be observable. Error bars are a combination of the variability in contrail properties due to seasonal ~~and diurnal~~ effects (also shown independently), and uncertainty in the derived threshold based on the observable proportion using 0.25 and 0.75 ~~P_{obs}~~ p_{obs} thresholds.

of these cases are instead limited by detection algorithm thresholds, and ultimately imager noise. Similarly, the decrease in resolution from the even-coarser 7 km resolution imager is relatively modest, but the proportion 'too optically thin' decreases in favour of the population 'too narrow' to be detected. This is a result of the specific detection algorithm applied—the coarser images are better-suited for detecting theoretical very wide contrails, so the upper-limit on contrail width that is theoretically detectable is relaxed, and the detectability threshold can be defined in some more optically-thin bins.

~~(78 ± 3)~~ Detectable contrails contribute (70 ± 2) % of ~~absolute net contrail forcing is theoretically observable~~ the net radiative forcing in simulated 2 km resolution images (Fig. 7). ~~This means~~ The detectability of forcing is higher than the detectability of contrail segments, meaning that the contrails with stronger radiative forcing are a more observable population than the ~~wider contrail population~~ population as a whole. This aligns with expectation: a small percentage of strongly-forcing contrails contribute most of the net warming (Teoh et al., 2022a), and more optically thick contrails tend to warm strongly (Meerkötter et al., 1999).

~~Contrails that have a strong LW forcing are typically more observable than those with a strong SW forcing. This is because the cooling (SW-forcing) population tends to consist of narrower (younger) contrails. This is visible by comparing the SW-dominant and LW-dominant regions of the net forcing CoCiP population in Fig. 5. This may be caused in part by the combination of~~ This interpretation is also consistent with the findings that the observable fraction of contrail forcing does not vary significantly much with imager resolution or by component of forcing (because the few optically thick contrail segments

causing much of the ~~daytime-only nature of SW forcing and the daytime bias of air traffic (Schumann and Heymsfield, 2017). As a result, the discrepancy between LW and SW components is less in the higher-resolution imager~~forcing are sufficiently wide that the resolution dependence is less significant).

The uncertainties given are a combination of ~~the P_{obs}~~a p_{obs}-derived threshold uncertainty ~~(described in Section 2.2) and the seasonal and dirunal variability (described in Section 2.3~~and seasonal variability. The p_{obs} uncertainty describes variations in the observability threshold, and is derived based on the different realisations of the imager noise field. The range is based on the proportion observable if the threshold is defined based on $p_{obs} > 0.25$ and $p_{obs} > 0.75$ conditions (i.e. detectable or undetectable in only one of the four realisations of the synthetic image). The ~~component due to seasonal and diurnal variability is also shown independently on Fig. 7. The combined uncertainty is dominated by the seasonal and dirunal component, indicating that the observability threshold is well-defined with respect to different realisations of the noise field~~impact of seasonal variability is assessed by taking the standard deviation of the observable fraction obtained when subsetting CoCiP population 1 based on the month of the year. Both the combination of the two uncertainties, and the uncertainty due to variability are shown in Fig. 7, and the variability in contrail properties clearly dominates the component due to instrument noise in this idealised case.

4.1.2 Speculative relaxation of limits imposed by the detection algorithm

The contrail observability is dependent on the contrail detection algorithm used. The observability threshold (derived in Section 3.2) is based on the lowest width for which a set of ~~of~~ optical-thickness-driving microphysical properties (i.e. r_{eff} and ~~IWP~~IWP_0) produces simulated brightness temperature field in which the contrail is detected using the ~~Mannstein et al. (1999)-like~~ detection algorithm introduced in Section 2.2. The algorithm used contains thresholds ~~as distributed with McCloskey et al. (2021),~~ tuned on human-labelled datasets to ~~maximise precision and recall—making these results reflect the contrails which would be observable as distinct objects by~~ optimise precision and recall, as distributed with McCloskey et al. (2021). Real contrails which were not identified by the human labellers would be spuriously considered 'false positives' if picked up by the detection algorithm. This means that the algorithm reflects the contrails theoretically observable by the human labellers. ~~A~~ Mannstein et al. (1999) chose a brightness temperature difference threshold uniquely low compared to existing algorithms at the time (0.2 K), and much lower than the threshold in the tuned algorithm (1.33 K), aiming to use the contrail's geometry rather than thresholding to ensure reliability.

As a test, a less-conservative detection algorithm was ~~tested, based on reducing the threshold~~ constructed by reducing applied thresholds from the human-labelled tuned ~~value~~ values to the least-conservative between ~~this and the value identified~~ these and the values used by Mannstein et al. (1999). ~~The~~ It should be noted that such an algorithm poses an increased risk of false positive detection so may only be practically applied when this risk can be reduced (such as the targeted observation of a contrail known to exist, or suspected to exist in a timestep following one where it is more confidently detectable). The algorithm of Mannstein et al. (1999) was designed for use with a different imager, so such algorithm adjustments need testing for their specific application. When applied to 10000 realisations of the clear sky instrument noise field (i.e. synthetic image with no contrail) no false positive detections occurred using this new algorithm, indicating that it is suitable to speculate on potential achievable detectabilities, albeit in this very controlled case. The threshold derived using this ~~adjustment~~ less-conservative

algorithm is shown with with an evolving contrail in Fig. 8(~~b~~d). In this case—using the same high-width adjustment of Section 3.2—(89 ± 1) % of segments and more than ~~95~~99 % of all components of forcing is theoretically observable in fields simulated with 2 km resolution. ~~This~~

Observation-independent ground truth data does not exist, so these detectabilities are unachievable for general observation (because false positives cannot be controlled for). However, this initial analysis suggests that the observability limit derived here can be relaxed if the risk of false positives can be ~~avoided~~mitigated, for example in the case of targeted observation of specific contrails based on advected flight tracks, where a likely location of the contrail is known.

4.1.3 Significant limitations imposed by more-complex backgrounds

To illustrate the significant impact caused by background cloud—and demonstrate that this is a maximum accessible fraction of contrails, the observability of contrails has been tested against a layer of background cirrus. ~~The cirrus layer~~ Additional radiative transfer simulations are made for this case. The background cirrus layer is 500 m deep, at 8 km altitude, with an effective radius of 5 µm (chosen as the intersection of the two ice cloud parameterisations due technical limitations) and IWP of 25 gm^{-2}. The layer has an optical thickness of approximately 3.

The cirrus layer significantly reduces the brightness temperature contrast between the contrail and the background, decreasing contrail detectability. Detectability has been tested using the same detection algorithm thresholds based on human-labelled datasets described in Section 2.2. Under this analysis, fewer than 2 % of contrail segments in ~~the instantaneous sample~~ CoCiP population 1 were detectable, and less than ~~5~~3 % of each component of forcing. The derived minimum-width threshold for observability is illustrated in Fig. 8(~~c~~e). Only ~~significantly more~~ the most optically-thick contrails were detectable. ~~A high-IWP limit of detectability seen in this observability threshold (as in of Section 3.1, Fig. 3(b))~~The minimum width required for detection shows a discontinuity at ~~high-IWP.~~ high-IWP_0, similar to the limit in Fig. 3(b). In this case the combination of background cirrus and contrail causes does not cause a brightness temperature difference signal at the centre of the contrail as it is sufficiently optically thick to be opaque in both the channels that are differenced. ~~Wider contrails with similar optical thickness are detected, because less-optically-thick parts of the contrail exist which remain detectable.~~ The high-IWP_0 discontinuity in the threshold does not completely prevent detection, but significantly increases the minimum detectable width. This is because the IWP profile (eq. 1) varies gradually-enough in wide contrails that their edges remain detectable.

The chosen effective radius (due to technical limitations) would be relatively unphysical for a midlatitude natural cirrus layer (although it may represent, for example, observation against a contrail cirrus outbreak). To provide a comparison, a similar test against a 30 µm cirrus layer has also been performed for contrails whose r_{eff} is high enough that radiative transfer simulations can be made. The IWP has also been increased to approximately maintain an optical thickness of 3. The derived threshold is shown in Fig. 8(f). Against this background, contrails with a higher effective radius become observable, demonstrating that this cirrus layer would pose less of an obstacle to contrail detection. From the data available for contrails below 10 µm, the two background cirrus thresholds appear comparable at lower effective radii.

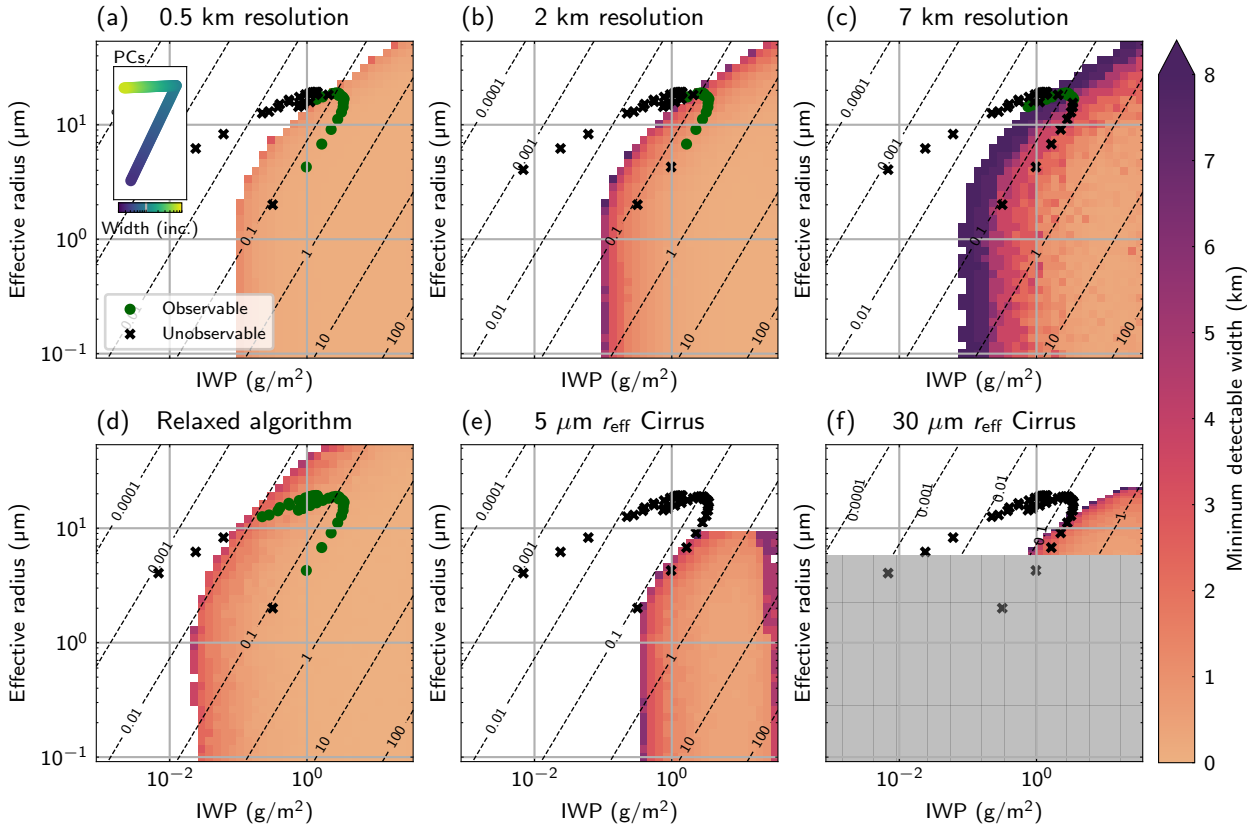

Figure 8. Representative trajectories of a contrail's evolution in parameter space against derived the minimum-width thresholds for detectability found in the course of this work. The ~~contrail IWP~~ IWP_0 and r_{eff} of a single contrail's evolution at each model timestep is marked ~~against~~ the ~~minimum detectable width for a given observability test using detection algorithm~~ following different thresholds: ~~tuned to hand-labelled data – as distributed with McCloskey et al. (2021)~~ using the original algorithm on 0.5 km (a), 2 km (b), and 7 km (c) spatial resolution images, with the less-conservative thresholds ~~reduced to the least-conservative values between the Mannstein et al. (1999) and McCloskey et al. (2021) implementations (unachievable for passive detection~~ discussed in ~~real data)~~ Section 4.1.2 (~~b~~d), and against ~~a layer~~ layers of background cirrus with 5 µm and 30 µm effective radii (~~e~~e, f). The same ~~detection algorithm~~ 2 km resolution imager of panel (b) is used for ~~panels~~ (~~a~~d–f)~~and (c)~~. Omitted effective radii in the case of 30 µm cirrus are due to technical limitations of the radiative transfer infrastructure. Also included (on inset axes to panel (a)) are the principal components identified in Section 3.3, coloured by their evolving width, which broadly correspond to the stages of contrail evolution~~(arrows)~~.

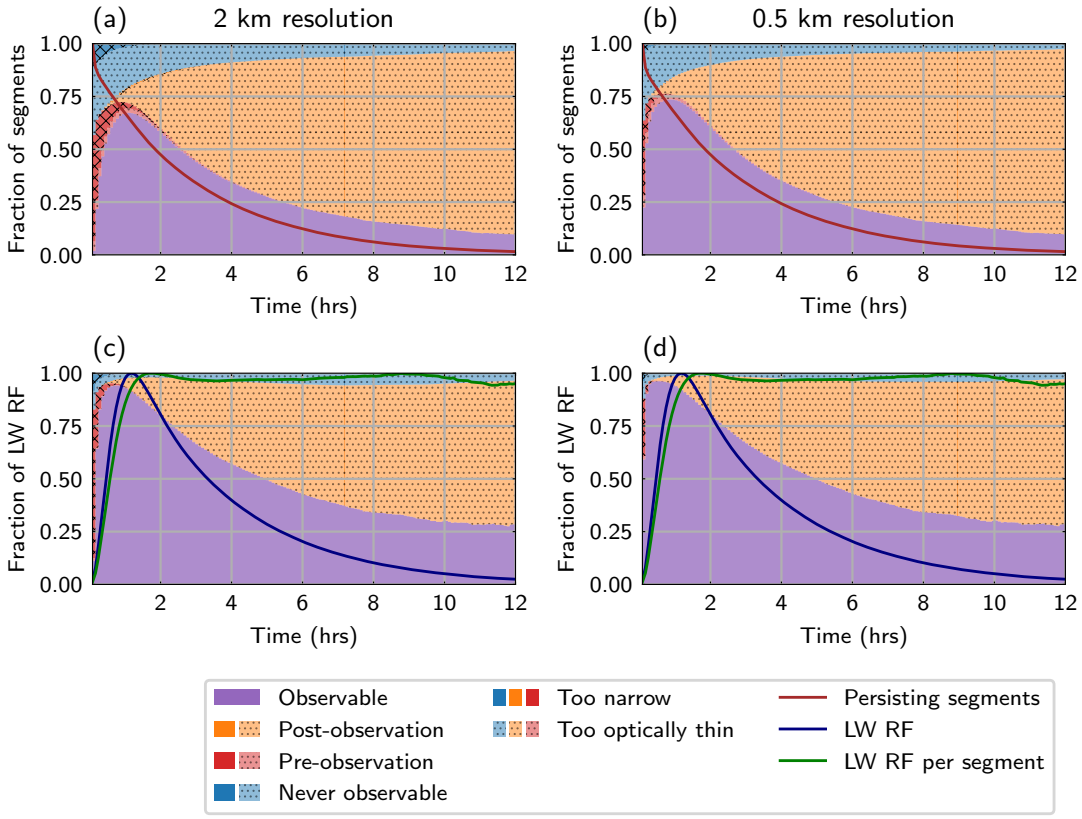

Figure 9. The time evolution of observability—the observability status of contrail segments (a, b) and of their proportions of forcing (c, d) formed globally within the time-evolving sample, using Jet-A1 fuel, for both 2 km (a, c) and 0.5 km (b, d) imagers. Using the adjusted observability threshold of Section 3.2 (Fig. 5; Fig. 8(a)), segments are categorised as 'observable', 'never observable', 'pre-observation' (have not yet been observable but will be observable later), or 'post-observation' (were observable earlier in their evolution, but are not at this age). Unobservable contrails have also been categorised as either too-narrow or too-optically-thin to be observed. Lines indicate: the number of persisting contrail segments (a,b), LW forcing (c,d), and the per-segment-mean LW forcing (c, d) due to contrails of a given age (relative to other CoCiP population 2 age-bins).

4.2 Observability with contrail aging

A contrail's properties evolve as it ages, so observability also has characteristic evolution. The evolution of one contrail from ~~the time-evolving sample (~~CoCiP population 2 ~~)~~ is shown against the different observability thresholds ~~derived is shown~~ of this work in Fig. 8 ~~.~~ This behaviour is typical of ~~the time-evolving dataset~~a contrail's time evolving properties. The stages of the

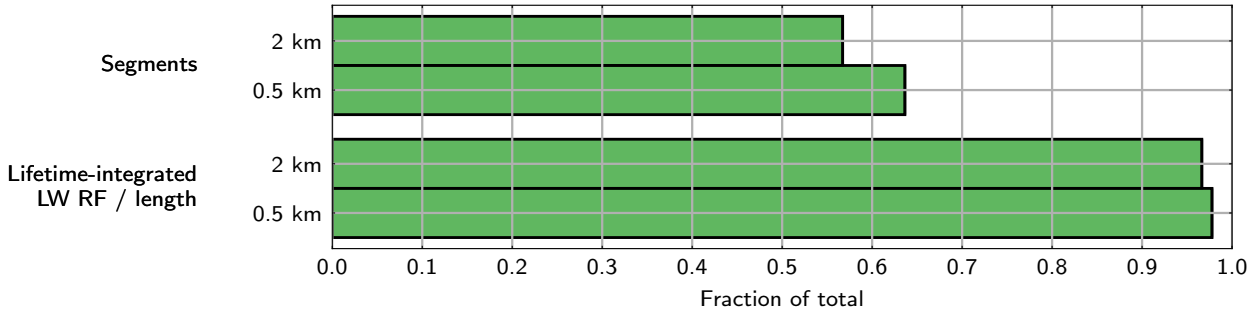

Figure 10. The proportion of ~~time-evolving~~ CoCiP population 2 contrails (and contrail EF/length) observable for at least one model timestep, as determined using contrail detection algorithm threshold tuned on hand-labelled data (the algorithm as distributed with McCloskey et al. (2021)).

contrail's evolution (growth, persistence, and dissipation) broadly align with the two PCs identified to explain a large proportion of the variance in CoCiP population 1 (Section 3.3). The observability status of the contrail is ~~marked—examining Fig. 8(a), at~~ marked—at formation it is initially too narrow to be observed, but as it grows the minimum observable width threshold is crossed, and the contrail becomes observable ~~.~~ (except when imaged against background cirrus, Fig. 8(e,f)). During the persistence phase, the contrail spreads over a wider area, decreasing ~~the IWP of the contrail~~ IWP_0 at approximately constant ~~effective radius~~ r_{eff}. During this time this contrail becomes unobservable, due to being too optically thin. Finally, this contrail dissipates, with ice crystals eventually decreasing in size, until it is removed from the model population at its 'end of life'. ~~Fig. 8(b,c) repeat the parameter-space trajectory and observability status using a less-conservative algorithm and when observed against a layer of background cirrus respectively (the thresholds as described in Section 4.1).~~

Fig. 9 shows the proportion ~~contrails which are observable as they age in the time-evolving sample (~~of contrail segments with different ages that are observable CoCiP population 2 ~~)~~ along with the proportion of the LW forcing. Each contrail segment has been tracked for its entire CoCiP ~~lifecycle~~ persistence lifetime (which was capped at 12 h), and observability has been assessed at each timestep. Data is binned based on model timesteps since formation, that is, contrails in the first bin were formed between 0 and 5 minutes ago and have survived until the time at which the model outputs data. This means that some contrails with persistence lifetime less than 5 minutes are never represented in the analysis, similar to the population of contrails captured in regular satellite observations.

~~Using the adjusted observability threshold of Section 3.2 (Fig. 5; Fig. 8(a)), contrail segments have been categorised as either theoretically observable (purple), or unobservable (red, orange, and blue). Unobservable contrails are either never observed with this imager before their dissipation (blue), have not yet been theoretically observable but will be observable later in their lifecycle (red), or have been previously observable but are no longer (orange). Unobservable contrails have again been categorised as either too narrow (full coloured and hashed)or too optically thin to be observed (muted colours and dotted).~~ LW forcing has been used, because its positive definite nature simplifies calculations and reduces variability in forcing estimates due to solar zenith angle (meaning the results are instead focussed on the link between contrail properties and radiative importance).

A small number of contrail segments are temporarily unobservable after their period of observation; these are classified as ‘~~post-observable’ while unobservable—this~~ post-observation’—this affects 8 % of segments in the 2 km imager and 7 % in the 0.5 km imager.

Each of the panels ~~are overplotted with relevant integrated quantities. The surviving proportion of segments is shown in Fig. 9(a,b) and the instantaneous LW~~ of Fig. 9 is overplotted with the relative contribution of contrails with a given age to the instantaneous population of contrails. Specifically, the proportions of contrail segments are shown alongside the fraction of persisting segments, equivalent to the fraction of segments that would be expected to be a given age for a given time. The proportions of forcing are shown with the contribution of contrails with a given age to the instantaneous global forcing due to contrails (as well as the per-segment mean forcing of contrails with a given age, approximately equivalent to the relative forcing per unit length ~~(both integrated over the surviving contrails and per contrail) is shown on Fig. 9.~~ of contrails with a given age).

The population of contrail segments decays with the dissipation of contrails (with a characteristic e-folding lifetime of around 3 h). Note that the ~~per-segment forcing per unit length peaks at~~ forcing per segments peaks just less than two hours after formation, remaining at this value for the remainder of the ~~persistance, although the total decays~~ persistence, as an increasingly optically thin contrail spreads over a broadening width. The total LW forcing decays much like the number of persisting segments, as some contrails dissipate~~(Fig. 9(c, d)).~~ .

The population of never-observable contrails ~~(blue)~~ consists of both ~~narrow and optically thin~~ too-narrow and too-optically-thin contrails. This population is much reduced in the forcing-weighted analyses (Fig. 9(c,d)), suggesting that keeping track of these contrails is less important for monitoring the radiative forcing. ~~For trials attempting to mitigate the formation of contrails~~However, it is ~~important that these contrails are avoided as they would lead to false negatives—inference ofno contrail when one has actually formed~~apparent that the formation (or lack of) of a significant proportion of contrail segments would not be validatable using satellite-borne imagers.

Pre-observable contrails tend to be too narrow to be observed, becoming observable when they have broadened sufficiently. A pre-observable population persists into the forcing-weighted case, ~~so these contrails also play an important radiative role. The~~ but the high-resolution imager provides a significant improvement in accessing this population.

When the contrails are no longer observable, they are overwhelmingly more likely to be too optically thin than too narrow. It is at this stage that contrail observability appears to decouple from the contrail lifetime—the post-observable phase doesn’t seem to be a transient phase as the contrail dissipates, but a growing proportion of the contrails. Again, it should be noted that the number of contrails and total ~~amount of~~ forcing are increasingly small with aging, so this increasing fraction remains relatively small as a fraction of the instantaneous population.

As a check for consistency with the analysis of Fig. 7, the ~~proportion of observable contrails has been integrated with the corresponding total~~ detection efficiencies of CoCiP population 2 contrails and of their RF have been estimated. This is performed by integrating the product of the observable proportion of contrails (or of LW RF) with the persisting fraction of segments (or relative contribution to the total LW RF) over the time since contrail formation. Approximately 45 % of contrail segments are found to be theoretically observable with the 2 km imager, increased to 50 % for the 0.5 km resolution

imager; 69 % and 70 % of LW forcing is theoretically observable for the 2 km and 0.5 km resolutions respectively. ~~These are slightly smaller than the the values based on the instantaneous sample, Fig. 7.~~ Comparing to the variability ranges derived based on CoCiP population 1 (Fig. 7), these values are mostly within the ranges of uncertainty, with the exception on the forcing observability with the 0.5 km resolution (which lies only slightly below). This variability highlights that the ~~portion of observable segments lies within variability, and the observable fraction of LW forcing does not. This highlights that daily~~ day-to-day variability in contrail properties and estimated forcing is even more extreme than seasonal variability.

The number of CoCiP population 2 contrails observed at least at some point during their lifecycle ~~was also found~~ is plotted for both the model population of segments and the lifetime-integrated LW forcing per unit length in Fig. 10. Around 57 % of contrail segments are observable in 2 km resolution images for at least one model timestep during their evolution. This increases to 64 % with the 0.5 km resolution imager. When weighted by their lifetime-integrated LW energy forcing, this is increased to 97 % and 98 % for the 2 km and 0.5 km resolution fields respectively. Uncertainty in these values is expected to be dominated by seasonal ~~and diurnal uncertainty~~ variability (as in Fig. 7), and has not been calculated for ~~the time-evolving sample (~~CoCiP population 2 ~~)~~because it is limited to a single date.

Finally, the distribution of the times ~~at which a contrail~~between a contrail's formation and the time at which it first becomes observable are examined. This transition is highly skewed, so the median age of first observability is given, with the first and third quartiles ~~are given as an uncertainty range~~to give an impression of the variability. In 2 km resolution images, ~~detection first occurs at (21^{+73}_{-11}) min , whereas observation occurs at an age of (9^{+61}_{-4}) min~~ the median time for the onset of detectability occurs at 21 min with first and third quartiles at 10 min and 94 min. The onset occurs at a median 9 min after formation in hypothetical 0.5 km images (between 5 and 70 min quartiles). This is in good agreement with the delays to onset of ~~GOES~~ GOES-ABI (ca. 2 km resolution) observation reported by Chevallier et al. (2023); Gryspeerdt et al. (2024)~~.~~, although these studies do not capture the higher limits estimated here. This is likely due to the increased difficulty in matching observed contrails to generating flights when the delay to observation increases.

4.3 Observable lifetime as a proxy for radiative importance

Radiative forcing during the part of the lifetime for which a contrail is unobservable may be significant. A fraction of contrails has been found both before and after their period of observability, including when weighted by their forcing (Fig. 9). ~~Radiative importance conclusions~~ Comparisons of relative radiative importance drawn from observed contrail lifetime (such as in Gryspeerdt et al., 2024) therefore carry an implicit assumption that the factors influencing the period of observability also determine the persistence lifetime of the contrail. This assumption is threatened by the 'too optically thin' ~~post-observable fraction found here~~contrails found here, which have been shown to comprise a significant proportion of the aged contrail population. Previous contrail tracking studies have inferred contrail lifetime from observed lifetime, requiring assumptions about initial contrail spreading rates and the generalisation of observation-derived survival functions to unobserved parts of a contrails lifetime (Gierens and Vázquez-Navarro, 2018). The length of time for which a contrail appears in consecutive geostationary satellite images—the 'observable lifetime' of the contrail—is measurable, and may be a good proxy for lifetime radiative impact. We now examine the relationship between this observable lifetime and its lifetime radiative impact.

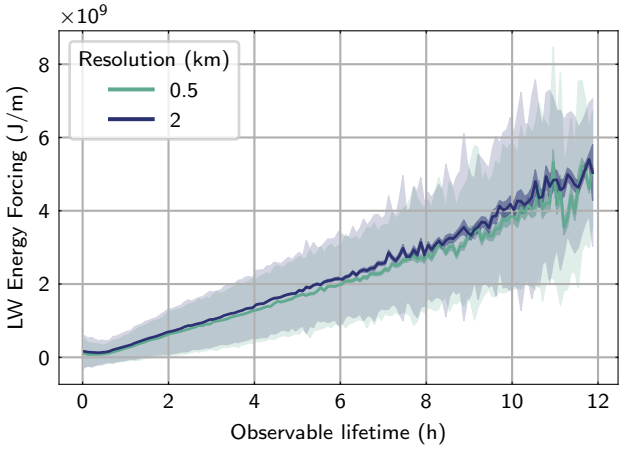

Figure 11. The relationship between lifetime-integrated energy forcing per unit length, and the observable lifetime. The ~~bold~~ strongly-shaded region denotes uncertainty in the mean, and the lightly-shaded region is the variability (the standard deviation for contrails with a given observable lifetime).

Fig. 11 shows the lifetime-integrated LW energy forcing per unit contrail length as a function of the theoretically observable lifetime for the contrails in the time-evolving sample. LW energy forcing is used (as in Section 4.2) rather than net forcing, so that net forcing variability due to the variations in SW forcing with time-of-day do not overwhelm the variability estimates. For both current imagers and theoretical higher-resolution imagers there is a positive correlation, with an approximately linear relationship between the observable lifetime and the LW radiative forcing for contrails observable for longer than 1 h.

There is significant variability in each observable lifetime bin, but a resolution dependence is well-resolved. Observed contrails tend to have higher lifetime forcing in more coarsely-resolved images. This follows from the ability of the 2 km resolution imager to only observe larger and more optically thick contrails, which in turn have stronger forcing.

4.4 Observability with the adoption of alternative fuels

Fig. 12 shows the potential observability consequences of decreased emission of activating ~~particulates—dominated by soot while~~ particulates—assumed to be dominated by soot as is the case for current fuels. The observability of a contrail population formed during fractional adoption of alternative fuels has been determined. The population results from CoCiP, run with identical flights and meteorology, but assuming a fractional adoption of SAF in the fuel in all aircraft (rather than Jet-A1 fuel) results in decreased ice emission indices. The modelling methodology follows that of the SAF experiments of Teoh et al. (2022b)—using the 30 %, 50 %, and 100 % SAF adoption experiments, which have been expanded to the global flight inventory of Teoh et al. (2024a).

There is a significant decrease in the observable fraction of contrail segments and forcing. In less a soot-rich environment, fewer contrail ice crystals are expected to form, so they grow larger (Voigt et al., 2021). A shift in the populations of Fig. 5 towards higher effective radius (and lower optical thickness) moves the contrails nearer the observability threshold, corre-

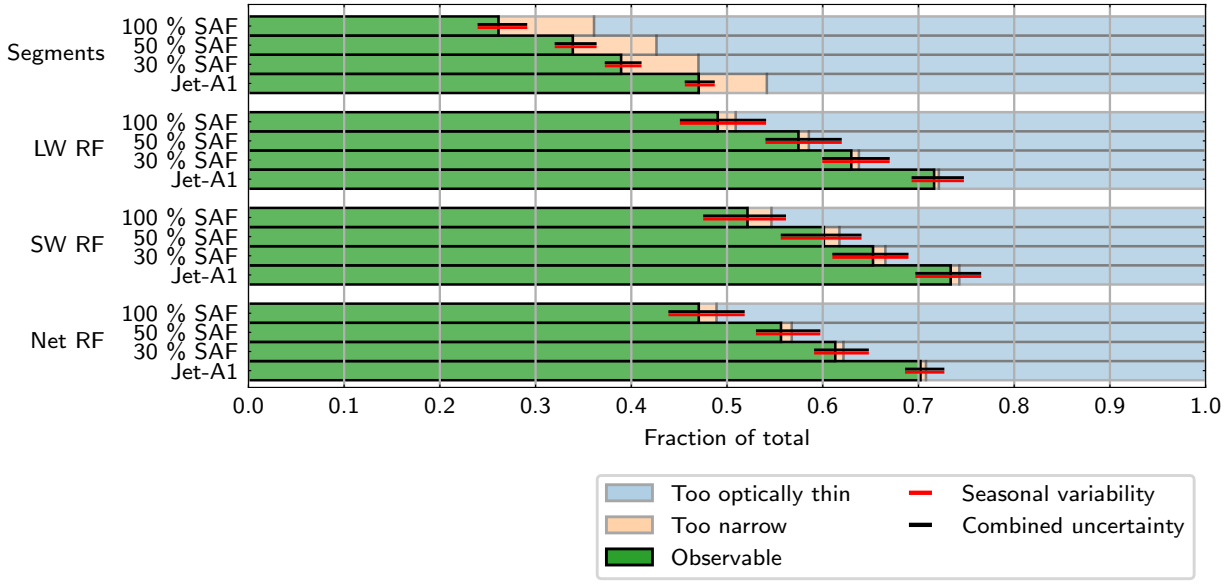

Figure 12. The theoretically observable fraction of contrail segments and instantaneous radiative forcing (as Fig. 7), based on ~~the~~ CoCiP ~~populations~~ population 1, assuming ~~a~~ fractional adoption of SAF biofuel leads to reduced effective emission of ice. ~~Observability has been tested for a simulated~~ A 2 km spatial resolution imager ~~for contrails in an otherwise clear sky~~is used.~~Error bars indicate the observable proportion using 0.25 and 0.75 P_{obs} thresholds.~~

sponding to these drops in observability. In simulated 2 km images after 100 % adoption, only (25 ± 3) % of segments are observable, and only ~~(58 ± 4)~~(47 ± 4) % of net forcing is theoretically observable. ~~Uncertainty is again dominated by seasonal and dirunal variability (as Fig. 7).~~ This means that coverage estimates for contrails produced by aircraft generating fewer non-volatile particulates will be based on fewer observations, making them (and potential assessments of radiative impact) more uncertain. The estimated uncertainty in detection efficiency is again dominated by seasonal variability (as Fig. 7).

Teoh et al. (2022b) explores the derived climate benefit of SAF adoption. It should be noted that, while a lower fraction of contrails is observable, there are also fewer contrail segments in the CoCiP population, and a reduced net contrail forcing. The activation of volatile particulates in less soot-rich exhaust (Ponsonby et al., 2024) has not been considered for this model population. Volatile activation would act to partially counteract the changes in observability driving the decreased observable fraction found here.

5 Discussion

5.1 Applicability of methodology

This analysis is limited to the very simple case of a straight-line contrails against a plain ocean background, with obstacles to observation from imager properties, and the thresholds from the algorithm applied. The algorithm, trained on hand-labelled contrails, provides insight into the contrails practically accessible in real satellite images~~(beyond~~. These are more-restricted than the absolute limits of detection in the artificial radiance fields ~~, imposed only~~ (which would only be imposed by imager resolution and noise) but are a good reflection of the best case possible when applied to real observations, because the algorithm restrictions reflect the limits of certainty against false positive detections.

The minimally-realistic synthetic contrails modelled here are intended as maximally-detectable test case. This approach is designed to establish whether some contrails go undetected with current instruments even in the most straightforward case. The approach also treats contrails as extended objects—testing not only that contrails produce a signal but that the extended signal is detectable as a contrail, aligning with detection methods that take the spatial properties of the contrail into account. The brightness temperature contrast, and particularly background inhomogeneity, has previously been noted to ~~be important for~~ limit the detection efficiency (Mannstein et al., 1999). Contrails imaged over land or against background cloud should be expected to be less observable than is established using this analysis because this will introduce additional features with reduced contrast to the brightness temperature fields used for detection, owing to their colder temperatures (particularly for underlying cloud) or reduced emissivity (particularly for surface features). A demonstration of the overwhelming impact background can have was made in Section 4.1.3, where an idealised cirrus layer obscured the detection of nearly all contrails. Conversely, observability may be increased when targeted observation of a contrail known to exist is possible (where a less-conservative detection algorithm could be applied, as discussed in Section 4.1.2). This is well-illustrated by the work of Vazquez-Navarro et al. (2010); Vázquez-Navarro et al. (2015), demonstrating that contrails detected using a higher-resolution non-geostationary imager enabled targeted observation in coarser-resolution geostationary observations for contrail evolution to be tracked. This tracking method also stands to enable the consideration of detected contrails beyond their initial linear phase.

Additional factors influencing contrail observability are likely to include contrail latitude, and ~~satellite~~ viewing zenith angle more generally, which would affect the dimensions of the imaged grid, and optical paths for radiative transfer (Maddux et al., 2010). These variations within regions of the same satellite field of view have not been considered, to simplify the parameter space and the analysis of unobservability causes. This also aligns the approach with the best-case observability. The analysis in this work is restricted also to a single atmospheric profile ~~(the US standard atmosphere~~and background (including surface temperature and emissivity). More-physical atmospheric profiles would also impact brightness temperature contrast slightly, but this smaller effect has not been treated here, again decreasing complexity and allowing more-direct consideration of the cause of detection limits. Additionally, the use of 1-D radiative transfer simulations neglects 3-D effects (Cornet et al., 2010).

Uncertainty in the derived threshold relative to instrument noise has been found to be small relative to seasonal ~~and diurnal~~ variations in the ~~instantaneous population of contrails~~ properties of CoCiP population 1 and their estimated radiative forcing. This highlights the importance of considering changes to contrail observability ~~in specific observational contexts~~due to their

actual background. The variability in observability has been found as a result of the changing contrail properties alone—not the varying meterology. It is clear that meterology will play a further role to enhance variability in detection efficiency, based on the adjusted threshold of Fig. 8(c) in the presence of background cirrus. Unconsidered uncertainties include innaccuracies in the CoCiP-derived population and contrail properties.

5.2 Relevance to applications of contrail observation

The fact that some contrails remain unobservable in these tests demonstrates that ~~these results are relevant considerations~~ detectability is a relevant consideration for observational applications, such as the observation of contrail radiative forcing. Fig. 7 indicates that ~~(22 ± 2)~~at least (30 ± 2) % of net contrail forcing goes unobserved ~~in~~ using current 2 km resolution geostationary imagers, and Fig. 5 shows that there is a microphysics dependence beyond a simple optical thickness threshold for observability. This is due to a combination of contrails whose observation is optical-thickness and resolution limited, of which, only the too-narrow contrails are accessible in theoretical higher-resolution images. As seen in Fig. 9(d) as compared to Fig. 9(c), this corresponds to the observation of contrails earlier in their evolution, should resolution be improved. Particular care is needed to compare contrail coverage when there is a change to contrail microphysics—such as in the adoption of biofuels, Fig. 11—where a change in observability may have been induced. Further caution is needed when comparing masked contrail grids on images with different resolution—in Fig. 3, different effective width values are measured when using different ~~imagers~~spatial resolutions.

One may seek to determine the efficacy with which contrail formation has been mitigated, for example, in a trial attempting to avoid forming contrails (Molloy et al., 2022). For this, effective flight matching is required as well as efficient detection, as described in ~~Geraedts et al. (2023)~~Geraedts et al. (2024). It has been shown that the majority of instantaneous forcing is theoretically observable using current instruments (Fig. 5), when tested in the ideal case shown here. ~~Futhermore~~Furthermore, in Section 4.2, 97 % of lifetime-forcing weighted contrail segments are shown to observable at least for some time in their evolution. This provides reassurance that most of the most climate-relevant contrails are observable at some time during their lifecycle. Effective flight matching relies on the detection of contrails shortly after their formation—to minimise any errors that develop between advected flight path and detected contrail. Here a higher-resolution contrail detection technique ~~makes~~ would make a significant difference—most contrails are detectable within 9 min of their formation (Section 4.2), compared to 21 min for the 2 km imager.

A final application in need of improved contrail observation is the validation of contrail models, a need laid out by Schumann et al. (2017) and Kärcher (2018). The thresholds derived here form a foundation to consider which contrails are observable and how many may need to be observed to draw confident conclusions about the predictive power of the models. These validation tasks often then require retrieval of the contrail cirrus properties and variability beyond just the simple detection of contrail coverage. Care is required in applying instruments to this task, illustrated by the varying effective widths measured for the same contrail imaged at different resolutions, Figs. 2 and 3.

6 Conclusions

Infrared imagers carried by geostationary ~~satelllites~~ satellites are well-placed to make widespread observations of the time-evolving properties of contrails. The detection of contrails is limited both early and late in their evolution: imaged radiance fields are coarsely resolved with respect to the geometry of young contrails, and aged contrails are wide and disperse. This work highlights the contrails that should not be expected to appear in images from geostationary satellites, even in the most ideal conditions, as a function of contrail properties and detection methods.

Satellite contrail observation has been simulated for simple straight-line contrails with a Gaussian profile, against a plain background, laid out in Fig. 1. A Mannstein et al. (1999) style line filtering algorithm has been used to test the observability of contrails in these simulated radiance fields (Fig. 2) modelled with different properties. First, contrail width, ~~IWP~~IWP$_0$, r_{eff}, depth, and altitude were varied independently (Fig. 3). Altitude was not seen to be a major driver of unobservability, particularly at altitudes where contrails exist (Fig. 4). Then, an 'observability threshold' is found by covarying the properties which produced strong observability responses (~~IWP~~IWP$_0$, r_{eff}, and contrail width). The threshold is ~~shown relative to distributions of the properties of~~ applied to the distribution of these properties given by a model-derived population of contrails (~~Population~~ CoCiP population 1 of Section 2.3) ~~at three different constant widths (and their forcing)~~ and to their estimated forcing. The outcome of this observability test for contrails with three different widths is shown in Fig. 5.

The ~~observability threshold was applied to this modelled population of global contrails—determining the observability of the instantanous population based on a sample~~ detection efficiencies of contrail segments and their forcing was derived, based on this sample of contrails distributed in time of day and year (Fig. 7). The most radiatively important contrails are more likely to be theoretically observable than the population as a whole. The unobservable fraction of the instantaneous global population of contrails varies from ~~(54±2)~~(62±2) % (of contrail segments in ~~2~~7 km resolution images) to only ~~(13±2)~~(35±3) % (of ~~LW~~ SW forcing in 0.5 km images)~~, shown in Fig. 7.~~. The observability is strongly sensitive to the ~~the~~ background—a simple layer of background cirrus shifts the observability threshold to include only the most optically thick contrails (Fig. 8(c)), obscuring detection of almost all contrails in the population.

The threshold was also applied to the time-evolving properties of contrails (Fig. 8). By analysing contrail segments forming globally over a 24 h period (~~Population~~ CoCiP population 2 of Section 2.3) the evolving observability behaviour (Fig. 9) was derived. Most contrails are theoretically observable at least at some point in their evolution. Around 57 % are visible in current 2 km resolution imagers, comprising 97 % of the total radiative forcing from the contrail population (Fig. 10).

It has been shown that the average lifetime ~~radiative~~ energy forcing is a strong function of the observable lifetime for the contrail population forecast by CoCiP (Fig. 11). This relationship enables ~~radiative-importance-conclusions~~ comparisons of the radiative importance to be drawn from the length of time for which a contrail is observed. Factors not considered here may obscure this result, particularly the development of a contrail outbreak or other meteorological evolution.

Finally, these satellite observations' limitations are found to be increasingly important when assessing the efficacy of climate change mitigation strategies. It has been shown that widespread adoption of cleaner-burning fuels would lead to a significant drop in contrail observability~~, with a~~. A 20 percentage-point drop in the ~~observable fraction of net instantanous~~ detection

efficiency of net instantaneous contrail radiative forcing is expected under a modelled decrease in ice crystal number with the theoretical complete adoption of SAF (Fig. 12). This could lead to an overstatement in the benefit of the climate action if this is not considered (if detected contrails are treated as the only contrails)~~, or at least extrapolation~~. Even if controlled for, extrapolation of the total impact would then be based on a smaller observable fraction. Contrail observability should be considered when assessing any action on emissions or contrail mitigation.

This work ~~can be~~ stands to be be expanded to consider meteorological conditions—particularly contrail overlap with underlying cloud and contrail outbreaks—as an obstacle to observability. Observation away from the sub-satellite region has also been neglected. The impact of this effect is not straightforward. A higher viewing zenith angle reduces the effective resolution, reducing contrail observability assuming the same contrail properties and meteorology. However, the longer atmospheric path length will enhance the effective cloud optical depth, making thinner contrails easier to detect (Maddux et al., 2010). Other aspects of the observing system, such as the time of day observations are made, may bias the population of contrails which is observed. Additionally, more-physical ~~atmospheric profiles~~ cases may impact the brightness temperature fields observed. Granularity in aircraft and engine properties stands to be considered, beyond the simple fuel case examined here.

Nonetheless, this work should give confidence to the use of contrail observations using satellites—under best-case conditions, the most radiatively important contrails are strongly observable.

Code and data availability. CoCiP data is from Teoh et al. (2024a), which details input data sources. Radiative transfer code uses libRadtran (Emde et al., 2016) and pyLRT (Gryspeerdt and Driver, 2024). The contrail detection algorithm is adapted based on code released with McCloskey et al. (2021).

Author contributions. All the authors contributed to designing the study. OD performed the analysis and wrote the manuscript. EG and MS provided comments and suggestions.

Competing interests. The authors have no competing interests to declare.

Acknowledgements. This work has received funding from a Royal Society University Research Fellowship (URF/R1/191602) and the EPSRC Centre for Doctoral Training in Aerosol Science (EP/S023593/1).

We thank Roger Teoh (Imperial College London) and Zebediah Engburg (Breakthrough Energy), who provided access to global CoCiP data output for both Jet-A1 fuel and with modelled SAF adoption.

References

Agarwal, A., Meijer, V. R., Eastham, S. D., Speth, R. L., and Barrett, S. R. H.: Reanalysis-Driven Simulations May Overestimate Persistent Contrail Formation by 100%–250%, Environmental Research Letters, 17, 014 045, https://doi.org/10.1088/1748-9326/ac38d9, 2022.

Bakan, S., Betancor, M., Gayler, V., and Graßl, H.: Contrail Frequency over Europe from NOAA-satellite Images, Annales Geophysicae, 12, 962–968, https://doi.org/10.1007/s00585-994-0962-y, 1994.

Bodas-Salcedo, A., Webb, M. J., Bony, S., Chepfer, H., Dufresne, J.-L., Klein, S. A., Zhang, Y., Marchand, R., Haynes, J. M., Pincus, R., and John, V. O.: COSP: Satellite Simulation Software for Model Assessment, Bulletin of the American Meteorological Society, 92, 1023–1043, https://doi.org/10.1175/2011BAMS2856.1, 2011.

Buras, R., Dowling, T., and Emde, C.: New Secondary-Scattering Correction in DISORT with Increased Efficiency for Forward Scattering, Journal of Quantitative Spectroscopy and Radiative Transfer, 112, 2028–2034, https://doi.org/10.1016/j.jqsrt.2011.03.019, 2011.

Chevallier, R., Shapiro, M., Engberg, Z., Soler, M., and Delahaye, D.: Linear Contrails Detection, Tracking and Matching with Aircraft Using Geostationary Satellite and Air Traffic Data, Aerospace, 10, 578, https://doi.org/10.3390/aerospace10070578, 2023.

Cornet, C., C-Labonnote, L., and Szczap, F.: Three-Dimensional Polarized Monte Carlo Atmospheric Radiative Transfer Model (3DMCPOL): 3D Effects on Polarized Visible Reflectances of a Cirrus Cloud, Journal of Quantitative Spectroscopy and Radiative Transfer, 111, 174–186, https://doi.org/10.1016/j.jqsrt.2009.06.013, 2010.

Duda, D. P., Minnis, P., Khlopenkov, K., Chee, T. L., and Boeke, R.: Estimation of 2006 Northern Hemisphere Contrail Coverage Using MODIS Data: ESTIMATION OF 2006 NH CONTRAIL COVERAGE, Geophysical Research Letters, 40, 612–617, https://doi.org/10.1002/grl.50097, 2013.

Emde, C., Buras-Schnell, R., Kylling, A., Mayer, B., Gasteiger, J., Hamann, U., Kylling, J., Richter, B., Pause, C., Dowling, T., and Bugliaro, L.: The libRadtran Software Package for Radiative Transfer Calculations (Version 2.0.1), Geoscientific Model Development, 9, 1647–1672, https://doi.org/10.5194/gmd-9-1647-2016, 2016.

Gasteiger, J., Emde, C., Mayer, B., Buras, R., Buehler, S. A., and Lemke, O.: Representative Wavelengths Absorption Parameterization Applied to Satellite Channels and Spectral Bands, Journal of Quantitative Spectroscopy and Radiative Transfer, 148, 99–115, https://doi.org/10.1016/j.jqsrt.2014.06.024, 2014.

Geraedts, S., Brand, E., Dean, T. R., Eastham, S., Elkin, C., Engberg, Z., Hager, U., Langmore, I., McCloskey, K., Ng, J. Y.-H., Platt, J. C., Sankar, T., Sarna, A., Shapiro, M., and Goyal, N.: A Scalable System to Measure Contrail Formation on a Per-Flight Basis, https://doi.org/10.48550/arXiv.2308.02707, 2023.

Geraedts, S., Brand, E., Dean, T. R., Eastham, S., Elkin, C., Engberg, Z., Hager, U., Langmore, I., McCloskey, K., Ng, J. Y.-H., Platt, J. C., Sankar, T., Sarna, A., Shapiro, M., and Goyal, N.: A Scalable System to Measure Contrail Formation on a Per-Flight Basis, Environmental Research Communications, 6, 015 008, https://doi.org/10.1088/2515-7620/ad11ab, 2024.

Gierens, K. and Vázquez-Navarro, M.: Statistical Analysis of Contrail Lifetimes from a Satellite Perspective, Meteorologische Zeitschrift, 27, 183–193, https://doi.org/10.1127/metz/2018/0888, 2018.

Gierens, K., Matthes, S., and Rohs, S.: How Well Can Persistent Contrails Be Predicted?, Aerospace, 7, 169, https://doi.org/10.3390/aerospace7120169, 2020.

Gryspeerdt, E. and Driver, O.: pyLRT, Zenodo, https://doi.org/10.5281/zenodo.11626012, 2024.

Gryspeerdt, E., Stettler, M. E. J., Teoh, R., Burkhardt, U., Delovski, T., Driver, O. G. A., and Painemal, D.: Operational Differences Lead to Longer Lifetimes of Satellite Detectable Contrails from More Fuel Efficient Aircraft, 2024.

Jeßberger, P., Voigt, C., Schumann, U., Sölch, I., Schlager, H., Kaufmann, S., Petzold, A., Schäuble, D., and Gayet, J.-F.: Aircraft Type Influence on Contrail Properties, Atmospheric Chemistry and Physics, 13, 11 965–11 984, https://doi.org/10.5194/acp-13-11965-2013, 2013.

Kärcher, B.: Formation and Radiative Forcing of Contrail Cirrus, Nature Communications, 9, 1824, https://doi.org/10.1038/s41467-018-04068-0, 2018.

Kärcher, B., Burkhardt, U., Unterstrasser, S., and Minnis, P.: Factors Controlling Contrail Cirrus Optical Depth, Atmospheric Chemistry and Physics, 9, 6229–6254, https://doi.org/10.5194/acp-9-6229-2009, 2009.

Lee, D., Fahey, D., Skowron, A., Allen, M., Burkhardt, U., Chen, Q., Doherty, S., Freeman, S., Forster, P., Fuglestvedt, J., Gettelman, A., De León, R., Lim, L., Lund, M., Millar, R., Owen, B., Penner, J., Pitari, G., Prather, M., Sausen, R., and Wilcox, L.: The Contribution of Global Aviation to Anthropogenic Climate Forcing for 2000 to 2018, Atmospheric Environment, 244, 117 834, https://doi.org/10.1016/j.atmosenv.2020.117834, 2021.

Lee, T. F.: Jet Contrail Identification Using the AVI-IRR Infrared Split Window, Journal of Applied Meteorology and Climatology, 28, 993–995, https://doi.org/10.1175/1520-0450(1989)028<0993:JCIUTA>2.0.CO;2, 1989.

Lever, J., Krzywinski, M., and Altman, N.: Principal Component Analysis, Nature Methods, 14, 641–642, https://doi.org/10.1038/nmeth.4346, 2017.

Maddux, B. C., Ackerman, S. A., and Platnick, S.: Viewing Geometry Dependencies in MODIS Cloud Products, Journal of Atmospheric and Oceanic Technology, 27, 1519–1528, https://doi.org/10.1175/2010JTECHA1432.1, 2010.

Mannstein, H., Meyer, R., and Wendling, P.: Operational Detection of Contrails from NOAA-AVHRR-data, International Journal of Remote Sensing, 20, 1641–1660, https://doi.org/10.1080/014311699212650, 1999.

McCloskey, K., Geraedts, S., Van Arsdale, C., and Brand, E.: A Human-Labeled Landsat-8 Contrails Dataset, in: Climate Change AI, Climate Change AI, https://www.climatechange.ai/papers/icml2021/2, 2021.

Meerkötter, R., Schumann, U., Doelling, D. R., Minnis, P., Nakajima, T., and Tsushima, Y.: Radiative Forcing by Contrails, Annales Geophysicae, 17, 1080–1094, https://doi.org/10.1007/s00585-999-1080-7, 1999.

Meijer, V. R., Kulik, L., Eastham, S. D., Allroggen, F., Speth, R. L., Karaman, S., and Barrett, S. R. H.: Contrail Coverage over the United States before and during the COVID-19 Pandemic, Environmental Research Letters, 17, 034 039, https://doi.org/10.1088/1748-9326/ac26f0, 2022.

Meyer, R., Mannstein, H., Meerkötter, R., Schumann, U., and Wendling, P.: Regional Radiative Forcing by Line-Shaped Contrails Derived from Satellite Data: CONTRAIL RADIATIVE FORCING FROM SATELLITE DATA, Journal of Geophysical Research: Atmospheres, 107, ACL 17–1–ACL 17–15, https://doi.org/10.1029/2001JD000426, 2002.

Meyer, R., Buell, R., Leiter, C., Mannstein, H., Pechtl, S., Oki, T., and Wendling, P.: Contrail Observations over Southern and Eastern Asia in NOAA/AVHRR Data and Comparisons to Contrail Simulations in a GCM, International Journal of Remote Sensing, 28, 2049–2069, https://doi.org/10.1080/01431160600641707, 2007.

Minnis, P., Palikonda, R., Walter, B., Ayers, J., and Mannstein, H.: Contrail Properties over the Eastern North Pacific from AVHRR Data, Meteorologische Zeitschrift, 14, 515–523, https://doi.org/10.1127/0941-2948/2005/0056, 2005.

Molloy, J., Teoh, R., Harty, S., Koudis, G., Schumann, U., Poll, I., and Stettler, M. E. J.: Design Principles for a Contrail-Minimizing Trial in the North Atlantic, Aerospace, 9, 375, https://doi.org/10.3390/aerospace9070375, 2022.

Ng, J. Y.-H., McCloskey, K., Cui, J., Brand, E., Sarna, A., Goyal, N., Van Arsdale, C., and Geraedts, S.: OpenContrails: Benchmarking Contrail Detection on GOES-16 ABI, http://arxiv.org/abs/2304.02122, 2023.

NOAA: GOES-R Series Data Book, https://www.goes-r.gov/downloads/resources/documents/GOES-RSeriesDataBook.pdf, 2019.

Palikonda, R., Minnis, P., Duda, D. P., and Mannstein, H.: Contrail Coverage Derived from 2001 AVHRR Data over the Continental United States of America and Surrounding Areas, Meteorologische Zeitschrift, 14, 525–536, https://doi.org/10.1127/0941-2948/2005/0051, 2005.

Ponsonby, J., King, L., Murray, B. J., and Stettler, M. E. J.: Jet Aircraft Lubrication Oil Droplets as Contrail Ice-Forming Particles, Atmospheric Chemistry and Physics, 24, 2045–2058, https://doi.org/10.5194/acp-24-2045-2024, 2024.

Sausen, R., Hofer, S., Gierens, K., Bugliaro, L., Ehrmanntraut, R., Sitova, I., Walczak, K., Burridge-Diesing, A., Bowman, M., and Miller, N.: Can We Successfully Avoid Persistent Contrails by Small Altitude Adjustments of Flights in the Real World?, Meteorologische Zeitschrift, https://doi.org/10.1127/metz/2023/1157, 2023.

Schumann, U.: On Conditions for Contrail Formation from Aircraft Exhausts, Meteorologische Zeitschrift, 5, 4–23, https://doi.org/10.1127/metz/5/1996/4, 1996.

Schumann, U.: A Contrail Cirrus Prediction Model, Geoscientific Model Development, 5, 543–580, https://doi.org/10.5194/gmd-5-543-2012, 2012.

Schumann, U. and Heymsfield, A. J.: On the Life Cycle of Individual Contrails and Contrail Cirrus, Meteorological Monographs, 58, 3.1–3.24, https://doi.org/10.1175/AMSMONOGRAPHS-D-16-0005.1, 2017.

Schumann, U., Mayer, B., Graf, K., and Mannstein, H.: A Parametric Radiative Forcing Model for Contrail Cirrus, Journal of Applied Meteorology and Climatology, 51, 1391–1406, https://doi.org/10.1175/JAMC-D-11-0242.1, 2012.

Schumann, U., Penner, J. E., Chen, Y., Zhou, C., and Graf, K.: Dehydration Effects from Contrails in a Coupled Contrail–Climate Model, Atmospheric Chemistry and Physics, 15, 11 179–11 199, https://doi.org/10.5194/acp-15-11179-2015, 2015.

Schumann, U., Baumann, R., Baumgardner, D., Bedka, S. T., Duda, D. P., Freudenthaler, V., Gayet, J.-F., Heymsfield, A. J., Minnis, P., Quante, M., Raschke, E., Schlager, H., Vázquez-Navarro, M., Voigt, C., and Wang, Z.: Properties of Individual Contrails: A Compilation of Observations and Some Comparisons, Atmospheric Chemistry and Physics, 17, 403–438, https://doi.org/10.5194/acp-17-403-2017, 2017.

Shapiro, M., Engberg, Z., Teoh, R., Stettler, M., and Dean, T.: Pycontrails: Python Library for Modeling Aviation Climate Impacts, Zenodo, https://doi.org/10.5281/zenodo.10182539, 2023.

Shenk, W. E. and Salomonson, V. V.: A Simulation Study Exploring the Effects of Sensor Spatial Resolution on Estimates of Cloud Cover from Satellites, https://journals.ametsoc.org/view/journals/apme/11/1/1520-0450_1972_011_0214_assete_2_0_co_2.xml, 1972.

Teoh, R., Schumann, U., Majumdar, A., and Stettler, M. E. J.: Mitigating the Climate Forcing of Aircraft Contrails by Small-Scale Diversions and Technology Adoption, Environmental Science & Technology, 54, 2941–2950, https://doi.org/10.1021/acs.est.9b05608, 2020.

Teoh, R., Schumann, U., Gryspeerdt, E., Shapiro, M., Molloy, J., Koudis, G., Voigt, C., and Stettler, M. E. J.: Aviation Contrail Climate Effects in the North Atlantic from 2016 to 2021, Atmospheric Chemistry and Physics, 22, 10 919–10 935, https://doi.org/10.5194/acp-22-10919-2022, 2022a.

Teoh, R., Schumann, U., Voigt, C., Schripp, T., Shapiro, M., Engberg, Z., Molloy, J., Koudis, G., and Stettler, M. E. J.: Targeted Use of Sustainable Aviation Fuel to Maximize Climate Benefits, Environmental Science & Technology, 56, 17 246–17 255, https://doi.org/10.1021/acs.est.2c05781, 2022b.

Teoh, R., Engberg, Z., Schumann, U., Voigt, C., Shapiro, M., Rohs, S., and Stettler, M. E. J.: Global Aviation Contrail Climate Effects from 2019 to 2021, Atmospheric Chemistry and Physics, 24, 6071–6093, https://doi.org/10.5194/acp-24-6071-2024, 2024a.

Teoh, R., Engberg, Z., Shapiro, M., Dray, L., and Stettler, M. E. J.: The High-Resolution Global Aviation Emissions Inventory Based on ADS-B (GAIA) for 2019–2021, Atmospheric Chemistry and Physics, 24, 725–744, https://doi.org/10.5194/acp-24-725-2024, 2024b.

Vazquez-Navarro, M., Mannstein, H., and Mayer, B.: An Automatic Contrail Tracking Algorithm, Atmospheric Measurement Techniques, 3, 1089–1101, https://doi.org/10.5194/amt-3-1089-2010, 2010.

Vázquez-Navarro, M., Mannstein, H., and Kox, S.: Contrail Life Cycle and Properties from 1 Year of MSG/SEVIRI Rapid-Scan Images, Atmospheric Chemistry and Physics, 15, 8739–8749, https://doi.org/10.5194/acp-15-8739-2015, 2015.

Voigt, C., Schumann, U., Minikin, A., Abdelmonem, A., Afchine, A., Borrmann, S., Boettcher, M., Buchholz, B., Bugliaro, L., Costa, A., Curtius, J., Dollner, M., Dörnbrack, A., Dreiling, V., Ebert, V., Ehrlich, A., Fix, A., Forster, L., Frank, F., Fütterer, D., Giez, A., Graf, K., Grooß, J.-U., Groß, S., Heimerl, K., Heinold, B., Hüneke, T., Järvinen, E., Jurkat, T., Kaufmann, S., Kenntner, M., Klingebiel, M., Klimach, T., Kohl, R., Krämer, M., Krisna, T. C., Luebke, A., Mayer, B., Mertes, S., Molleker, S., Petzold, A., Pfeilsticker, K., Port, M., Rapp, M., Reutter, P., Rolf, C., Rose, D., Sauer, D., Schäfler, A., Schlage, R., Schnaiter, M., Schneider, J., Spelten, N., Spichtinger, P., Stock, P., Walser, A., Weigel, R., Weinzierl, B., Wendisch, M., Werner, F., Wernli, H., Wirth, M., Zahn, A., Ziereis, H., and Zöger, M.: ML-CIRRUS: The Airborne Experiment on Natural Cirrus and Contrail Cirrus with the High-Altitude Long-Range Research Aircraft HALO, Bulletin of the American Meteorological Society, 98, 271–288, https://doi.org/10.1175/BAMS-D-15-00213.1, 2017.

Voigt, C., Kleine, J., Sauer, D., Moore, R. H., Bräuer, T., Le Clercq, P., Kaufmann, S., Scheibe, M., Jurkat-Witschas, T., Aigner, M., Bauder, U., Boose, Y., Borrmann, S., Crosbie, E., Diskin, G. S., DiGangi, J., Hahn, V., Heckl, C., Huber, F., Nowak, J. B., Rapp, M., Rauch, B., Robinson, C., Schripp, T., Shook, M., Winstead, E., Ziemba, L., Schlager, H., and Anderson, B. E.: Cleaner Burning Aviation Fuels Can Reduce Contrail Cloudiness, Communications Earth & Environment, 2, 1–10, https://doi.org/10.1038/s43247-021-00174-y, 2021.

Wolf, K., Bellouin, N., and Boucher, O.: Sensitivity of Cirrus and Contrail Radiative Effect on Cloud Microphysical and Environmental Parameters, Atmospheric Chemistry and Physics, 23, 14 003–14 037, https://doi.org/10.5194/acp-23-14003-2023, 2023.

Wu, X. and Schmidt, T.: GOES-16 ABI Level 1b and Cloud and Moisture Imagery (CMI) Release Full Validation Data Quality Product Performance Guide for Data Users, 2019.

Yang, P., Hong, G., Dessler, A. E., Ou, S. S. C., Liou, K.-N., Minnis, P., and Harshvardhan: Contrails and Induced Cirrus: Optics and Radiation, Bulletin of the American Meteorological Society, 91, 473–478, https://doi.org/10.1175/2009BAMS2837.1, 2010.

Yang, P., Bi, L., Baum, B. A., Liou, K.-N., Kattawar, G. W., Mishchenko, M. I., and Cole, B.: Spectrally Consistent Scattering, Absorption, and Polarization Properties of Atmospheric Ice Crystals at Wavelengths from 0.2 to 100 Mm, Journal of the Atmospheric Sciences, 70, 330–347, https://doi.org/10.1175/JAS-D-12-039.1, 2013.

Zhang, G., Zhang, J., and Shang, J.: Contrail Recognition with Convolutional Neural Network and Contrail Parameterizations Evaluation, Sola, 14, 132–137, https://doi.org/10.2151/sola.2018-023, 2018.